

Review

Recent Progress in Preparation and Anti-Icing Applications of Superhydrophobic Coatings

Yuebin Lin ^{1,*}, Haifeng Chen ², Guanyu Wang ³ and Aihui Liu ¹

¹ Faculty of Mechanical & Material Engineering, Huaiyin Institute of Technology, 1 Meicheng Street, Huaian 223003, China; liuah@hyit.edu.cn

² Department of Materials Chemistry, Qiuzhen School, Huzhou University, 759 East 2nd Road, Huzhou 313000, China; header@zjhu.edu.cn

³ College of Materials Science and Technology, Nanjing University of Aeronautics and Astronautics, 29 Yudao Street, Nanjing 210016, China; wangguanyu@nuaa.edu.cn

* Correspondence: lybzyt@hyit.edu.cn; Tel.: +86-517-8356-0091

Received: 9 January 2018; Accepted: 23 May 2018; Published: 31 May 2018



Abstract: Aircraft icing refers to ice formation and accumulation on the windward surface of aircrafts. It is mainly caused by the striking of unstable supercooled water droplets suspended in clouds onto a solid surface. Aircraft icing poses an increasing threat to the safety of flight due to the damage of aerodynamic shape. This review article provides a comprehensive understanding of the preparation and anti-icing applications of the superhydrophobic coatings applied on the surface of aircrafts. The first section introduces the hazards of aircraft icing and the underlying formation mechanisms of ice on the surface of aircrafts. Although some current anti-icing and de-icing strategies have been confirmed to be effective, they consume higher energy and lead to some fatigue damages to the substrate materials. Considering the icing process, the functional coatings similar to lotus leaf with extreme water repellency and unusual self-cleaning properties have been proposed and are expected to reduce the relied degree on traditional de-icing approaches and even to replace them in near future. The following sections mainly discuss the current research progress on the wetting theories of superhydrophobicity and main methods to prepare superhydrophobic coatings. Furthermore, based on the bouncing capacity of impact droplets, the dynamic water repellency of superhydrophobic coatings is discussed as the third evaluated parameter. It is crucial to anti-icing applications because it describes the ability of droplets to rapidly bounce off before freezing. Subsequently, current studies on the application of anti-icing superhydrophobic coatings including the anti-icing mechanisms and application status are introduced in detail. Finally, some limitations and issues related to the anti-icing applications are proposed to provide a future outlook on investigations of the superhydrophobic anti-icing coatings.

Keywords: wettability; icing; anti-icing; icephobicity; superhydrophobic coatings

1. Introduction

1.1. Hazards of Icing

Adhesion of ice and wet-snow on aircraft surfaces causes numerous serious aviation accidents and has become a fatal threat to flight safety. In November 2004, a flight (China Eastern Airlines MU5210) from Baotou to Shanghai crashed due to undesired ice accumulation on the surface of aircraft, causing serious economic issues and a huge loss of lives. The accident investigation further confirmed that ice accretion in frosting weather resulted in loss of control over operating speed and caused the plane to lose its lift, which reduced the critical angle of attack, especially when the ice was formed at the wing

leading edge. Coincidentally, in June 2006, KJ-200 early-warning aircraft belonging to the China Air Force was carrying out task on the way through the supercooled cloud area and gradually faced the ice accumulation on the surface of aircraft. This caused the aircraft to lose control and the crew died in the disaster. Furthermore, in June 2009, owing to the ice accretion on the surface of A330 aircraft, the airspeed system broke down, finally causing the aircraft to crash into the Atlantic Ocean. Therefore, aircraft icing has been a burning problem to confront for years.

Aircraft icing refers to ice formation and accumulation on the windward surface of aircrafts [1,2]. Once the ice is formed, the aerodynamic shape of aircraft is severely damaged; and the critical angle of attack also decreases. These changes lead to a series of serious flight problems, including the redistribution of airfoil pressure, reduction of lift factor, increase in resistance coefficient, and the rapid diminution of lift resistance ratio. Moreover, liftoff speed and running distance increase significantly and make taking-off and climbing difficult under icing conditions.

The airflow separation caused by ice on the aircraft tails is also a serious issue. It affects the handling speed of the aircraft rudder and reduces the aircraft pitch torque coefficient and the critical angle of attack of wing/tail, finally resulting in increment of the allowable speed when an aircraft is flying horizontally [3–5]. Furthermore, ice accretion on horizontal tails can easily lead to serious non-manipulative “aircraft bow” phenomenon when the aircraft takes off or lands. This is mainly attributed to the variation of the critical negative angle of attack. In general, the horizontal stabilizer remains at a negative angle of attack during taking-off or landing; and ice adhesion reduces the negative angle of attack. At this moment, airflow separation can occur at a smaller negative angle of attack when the aircraft is flying at a large speed or under fewer overloads. With the further increase in speed, the angle of attack further reduces. The complete separation of the airflow occurs below horizontal tail, closely following a non-manipulative “aircraft bow” phenomenon. At this point, to reverse this phenomenon, the pilot has to increase the deflection angle of wing flaps, while accelerating the separation of airflow [6].

On the other hand, ice accumulation on the engine inlet also easily causes thrust reduction and poor performance and surge. Once the engine inlets are frozen, the original streamline shape changes rapidly and additional resistance increases. Furthermore, the aerodynamic characteristics of the intake and compressor passages change, so that the airflow gets reduced, resulting in the gradual reduction of thrust. More seriously, the aircraft flameout in flight probably happens because the ice falls off and cracks into the engine blades with the assistance of airflow [7]. Moreover, ice accumulation on the aircraft surface similarly affects a variety of communication and sensing equipment, in particular, the detection of air pressure on the airspeed tubes, making the pilot misjudge the flight speed, weather conditions, and even neglect the handling of aircraft. In conclusion, aircraft icing has been recognized as a potential threat to aviation security, thus restricting the development of aviation industry and seriously affecting people’s normal life [8].

1.2. Mechanism of Ice Formation

Investigation of the serious security threat caused by icing, comprehensive understanding of the aircraft icing process, and development of efficient de-icing and anti-icing technologies have become important research topics for domestic and international aviation scientists. Based on the study of flight meteorological conditions, clouds in the atmosphere mainly contain three types of aqueous phases: solid ice crystals, supercooled water droplets, and water droplets. These phases change with the altitude and cloud temperature characteristics [9–11], as shown in Figure 1.

- Ice crystals: refer to the solid hydrate when water vapor grows up on the ice nucleus by deposition process. The aircraft icing is mainly dry icing, where ice crystals deposit directly on the surface of the aircraft.
- Supercooled water droplets: refer to the water droplets which still exist in the liquid form below the freezing point [12]. The main reason responsible for this phenomenon is that with the increase in height, the temperature drops rapidly below the freezing point. However, the droplets lack the

ice nucleation vectors so that the water droplets below the freezing point are still in a liquid form. The temperature range of these water droplets is typically between 0 and -40 °C. In this case, the aircraft icing is water droplets icing, and a high ice adhesion occurs on the solid surface of the aircraft.

- Ordinary water droplets: mainly refer to the water vapor which distributes in the clouds. Moreover, this type of water droplets generally exhibit below the flight height and they do not easily get frozen on the surface of the plane.

Ice crystals hit the surface below the freezing point without any changes in the phase compositions; therefore, a lower adhesion occurs between the formed ice and solid surface (it can be removed off under the action of its own gravity). In contrast, ice accumulation caused by supercooled water droplets is the most common form in aircraft icing process. In general, aircraft icing mainly refers to the process, where the supercooled water droplets first hit the aircraft surface, and the subsequent phase transition occurs to produce a high bonding strength between ice and substrate surface [13,14]. Under the action of fairly strong convective airflow, a wide area of dispersed supercooled water droplets appears in the air, which easily causes the freezing of the supercooled water droplets on the surface of aircrafts. As a consequence, aircraft icing mainly depends on the distribution of supercooled water droplets, liquid water content, mean effective diameter of supercooled water droplets, and airflow temperature. Although supercooled water droplets do not easily freeze in the clouds, they are very unstable, and even a smaller disturbance compels them to quickly freeze into ice. When aircrafts fly through such a cold region, supercooled water droplets hit the aircraft wing, propeller, and the fronts of engine and other parts, and are broken and spread on the surface. The surface curvature decreases suddenly, thus the pressure of liquid water is abruptly reduced, causing the increase in the relative freezing point [15–17]. Moreover, owing to low temperature of aircraft surface, the heat emitted by the droplets solidification process is absorbed quickly, which leads to the rapid freezing of the supercooled water droplets on the surface of aircrafts [18].

According to specific conditions of icing and different shapes of accumulated ice, aircraft icing is generally divided into the following three types: clear ice, rime, and mixed ice, as shown in Figure 2. Different ice shapes have different effects on performance of flight. The formation temperature of the clear ice is relatively high (generally higher than -10 °C); and the formed ice layer has a smooth and transparent surface with high density adhesion. Rime is mainly formed at a lower temperature (lower than -20 °C), at which the supercooled water droplets immediately release the latent heat and quickly freeze after hitting the substrate surface. Owing to extremely rapid freezing process, there is no enough time to remove air bubbles present between the ice particles, resulting in poor transparency and loose tissue of the ice layer. As a result, the rime displays lower ice adhesion strength on the substrate surface which is easy to be removed off. The mixed ice including both rime and clear ice is endowed with the characteristics of both the clear ice and the rime. The rime mainly distributes in the forefront of the ice layer, while transparent and dense clear ice mainly exists on both sides with higher ice adhesion strength [19,20].

To better cope up with the icing problem faced in the flight process, aircraft icing is divided into four grades, as listed in Table 1. In general, weak ice (micro-ice) does not pose threat to flight safety, unless the icing time is too long. This degree of icing rate is slightly larger than sublimation. Mild ice phenomenon appearing for more than 1 h brings some problems to flight safety. At this point, the necessary de-icing approaches should be used to eliminate potential threats. Strong ice (moderate ice) further increases the risks. In this case, anti/de-icing equipment must be operated to remove the ice from the surface of aircrafts. At the same time, pilots should consider whether to change the flight altitude or course. In the extremely strong ice (severe ice) condition, anti-icing equipment on the aircraft is not able to reduce or control ice accumulations. In this case, pilot must immediately change the course. It is noteworthy that the above-mentioned descriptions are not clear enough, because different types of aircrafts in the same environment have different reactions to the degree of icing.

For instance, the mild ice accretion formed on some large aircrafts may be a severe ice problem for a Cessna 150 aircraft.

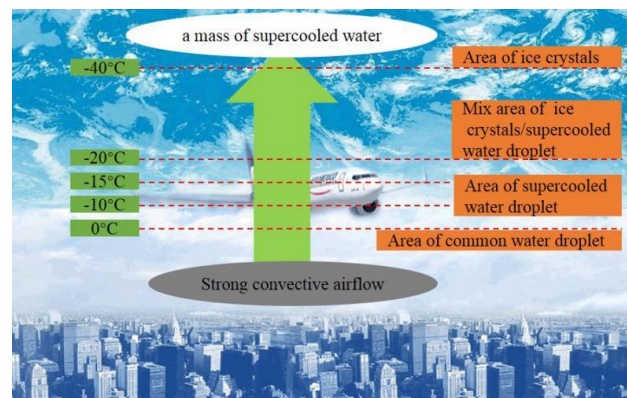


Figure 1. Distribution of ice crystals and supercooled water droplets in the clouds.

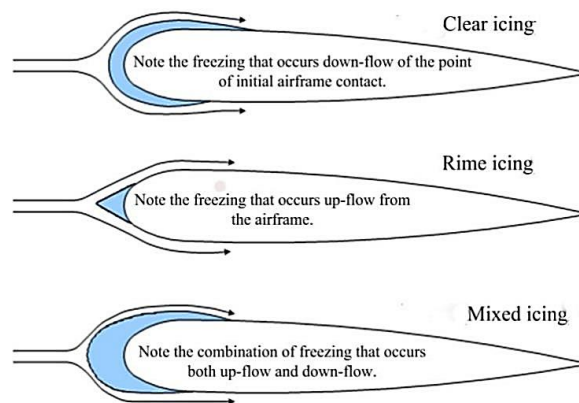


Figure 2. Three typical types of aircraft icing.

Table 1. Aircraft icing level classification.

Icing Grades		Ice Thickness Per Unit Time (mm min ⁻¹)	Ice Thickness of The Flight Process (cm)
Weak Ice	☞	<0.6	≤5.0
Mild Ice	☞☞	0.6–1.0	5.1–15.0
Strong Ice	☞☞☞	1.1–2.0	15.1–30.0
Extremely Strong Ice	☞☞☞☞	>2.0	>30.0

1.3. Anti-Icing and De-Icing Technologies

Facing different icing parts and types, it is urgent to develop some suitable anti-icing and de-icing methods. Aircraft anti/de-icing research has become one of the important factors to restrict the development of aviation industry in China [21–23]. Currently, engineers have adopted various approaches to achieve anti-icing or de-icing behavior, which are mainly divided into two categories. The one is the anti-icing system, which does not allow the complete production of ice on some parts of the aircraft surface. The other is de-icing system, which allows the accumulation of a small amount of ice, thus the de-icing approaches are definitely required. Common anti/de-icing technologies can be subdivided into mechanical, liquid, and thermal anti/de-icing systems, as shown Figure 3 [24,25]. Among them, according to different loading ways, the mechanical de-icing technologies can be divided into pneumatic de-icing and electric-pulse de-icing. Thermal anti-icing can

be further divided into electric anti-icing, air-thermal anti-icing, continuous anti-icing, and intermittent de-icing technologies [26]. They have different characteristics and working principles, which are discussed in the following section.

- Mechanical de-icing: Uses mechanical ways to break the ice and it mainly relies on the expansion pipes which are placed on the aircraft surface. When the aircraft surface is frozen, the accumulated ice can be broken under the assistance of inflated pipes, which then flows away due to the airflow. Furthermore, some electric-pulse technologies are also used to remove ice, which mainly depend on periodic vibration of the icing surface.
- Air thermal anti-icing: It is mainly used to solve the problem of modern transport aircrafts' wing and inlet icing and the heat is created by the engine compressor. When this system works, hot air after pressure regulation enters into the anti-icing pipes in front of the wing and tail. Hot air under certain pressure is squirted from the small pipe hole, finally leading to a high speed and a local low pressure. Air in the cavity is expelled from wingtip after mixing with the hot air, thus preventing ice accumulation on the surface of aircraft wings.
- Liquid de-icing: This process includes continuous spraying of the anti-icing fluids to reduce the freezing point, thus the water droplets do not easily freeze on the surface of aircrafts [27].
- Electric anti/de-icing: Through the resistance heating to prevent surface from icing, this system is commonly used on windshields, propellers, and airspeed tubes [28]. This process involves low power loss and uniform heating; therefore, electric–thermal anti-icing is widely used in modern large passenger aircrafts.

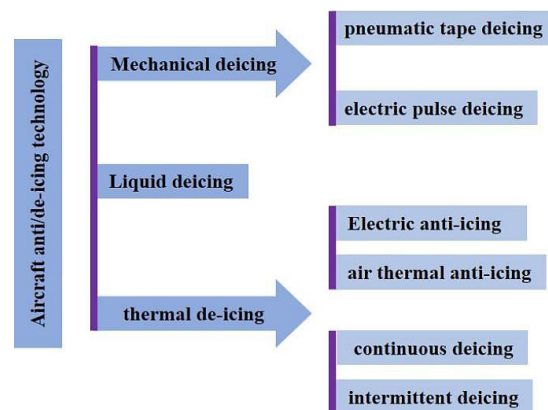


Figure 3. Aircraft anti/de-icing technologies.

Although the above-mentioned active anti-icing technologies are somewhat effective, some necessary anti/de-icing devices in turn increase the weight of aircraft and reduce the fuel efficiency, bringing many negative factors to the designers and manufacturers. Moreover, the safety and reliability of aircraft reduce significantly due to the thermal cycles and mechanical vibration conditions that surface metal suffers [29–31]. Therefore, based on the requirements of high safety and reliability to aircraft, especially to civil airliners, the traditional active anti/de-icing technologies offer some limitations. Thus, it is necessary to develop a new type of passive anti-icing technology. NASA Glenn Research Center has carried out the basic researches related to aircraft passive anti-icing technology, since as early as 2010. It is expected to use the intrinsic properties of materials to solve the problem of aircraft icing. According to the studies of surface functional modification of metal or polymer materials, the hydrophobic surface is beneficial to achieve the purpose of preventing icing.

The new perspective of passive anti-icing based on the surface modification principle is currently an important direction of development. Through surface modification of the material on the aircraft surface, researchers make the surface hydrophobic, expecting to solve the problem of aircraft icing

from the sources, and as far as possible to avoid the conventional anti/de-icing system design of aircrafts [32–35]. The analysis of aircraft icing process described above indicates that aircraft icing occurs mainly through supercooled droplets impacting and wetting the aircraft surface. Then the rapid heat exchange between the droplets and the solid surface causes the droplets to freeze on the surface of the aircraft. Therefore, a functional surface which is similar to lotus leaves can be fabricated on aluminum, titanium alloys, and other substrates (see Figure 4) by surface modification technologies. In this case, the water droplets cannot wet the solid surface; therefore, they get rapidly fallen off due to their own gravity and airflow [36–38]. Even if the droplets are frozen, the contact area between the solid surface and the ice is reduced, which leads to a lower ice adhesion because of this special non-wetting condition. Therefore, the ice easily falls down under the influence of the high-speed airflow [39,40]. Undeniably, a lot more systematic explorations are highly demanded to design and fabricate a functional superhydrophobic coating which is similar to the lotus leaf surface to meet the aircraft service conditions.



Figure 4. Superhydrophobic lotus leaf surface.

2. Surface Wettability for Superhydrophobicity

When liquid and solid contact with each other, the liquid expands outwards along the solid surface, and the original liquid–gas and solid–gas interfaces in the system are gradually replaced by the new type of solid–liquid contact interface, i.e., wettability [41,42]. Wettability is one of the most important characteristics of solid surface, and it can affect many physical and chemical processes, such as adhesion, adsorption, and lubrication. There are two main factors that affect the surface wettability: surface compositions that control surface free energy and microstructure that affects microscopic roughness [43,44]. Lower surface free energy can induce a smaller solid–liquid contact interface with a certain extent of non-wettability [45,46]. According to literature, hydrogen atoms in the polymer hydrocarbons are replaced by some low-energy atoms in favor of realizing the regulations of surface free energy [47]. It has been found that the use of fluorine atoms to replace hydrogen atoms can effectively reduce the surface free energy of polymers, and more fluorine atoms can cause lower surface free energy [48]. Nishino et al. found that the lowest surface free energy was about 6.7 mJ m^{-2} , and it was obtained using seventeen fluorine atoms to replace the silane atoms [49]. On such a smooth surface with the lowest surface free energy, water droplets still wet the surface with a maximum contact angle of $\sim 120^\circ$ [50]. Therefore, the subsequent researches mainly focus on the control of microstructure to further increase the surface non-wettability with higher water contact angle [51]. In this situation, it is necessary to discuss the main wetting theory models for the microscopic rough surface.

2.1. Wetting on the Ideally Smooth Surface—Young's Equation and Contact Angle

Wetting is the result of the stability of three-phase (gas, liquid, and solid) interfaces. Liquid on a given solid surface induces the formation of a stable system, and the tangents to the interfaces at the three-phase intersection point produce an angle θ (as shown in Figure 5), namely, contact angle. In the early nineteenth century, Young considered that the contact angle θ had a close relationship with the

three-phase interfacial tensions, and then Dupre further verified and proposed the famous Young's equation [52]:

$$\gamma_{sl} + \gamma_{lg} \cos \theta = \gamma_{gs} \quad (1)$$

where γ_{sl} is the solid–liquid interface tension, γ_{lg} is liquid–gas interface tension, and γ_{gs} is the gas–solid interface tension. The Young's contact angle is the equilibrium contact angle that a liquid makes with an ideal solid surface. For droplets or surfaces with very small radii of curvature deposited on the ideal surfaces, the equilibrium contact angle may be different due to line tension [53]. Moreover, the Young's contact angle depends only on the physicochemical nature of the three phases and it is independent of the droplet shape and external field under very general assumptions.

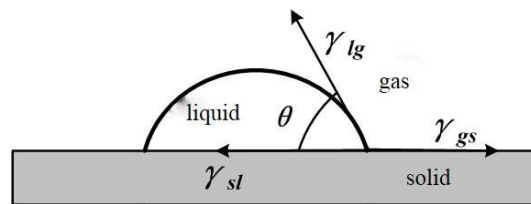


Figure 5. Schematic illustration of the contact angle of the liquid droplet on the surface.

Young's equation is the basis for the study of solid wettability, and the wetting degree can be effectively expressed in terms of the contact angle [54]:

- $\theta = 0$: Completely hydrophilic, the reference droplet spreads completely on the solid surface.
- $0 < \theta < 90^\circ$: Hydrophilic, smaller value of θ induces higher hydrophilicity.
- $90^\circ < \theta < 180^\circ$: Hydrophobic, the solid surface gets partially wetted by the reference droplets. Moreover, if the value of $\theta > 150^\circ$, then the surface is considered to be superhydrophobic.
- $\theta = 180^\circ$: Completely hydrophobic, the liquid is spherical on the solid surface.

It is noteworthy that Young's equation is applicable to the homogeneous chemical compositions and uniform and isotropic ideal surfaces, because in this case the liquid can form stable wetting contact interfaces.

2.2. Wetting on Non-Ideal Surfaces—Wenzel Equation

The actual surface of solid is often rough and uneven, and the chemical compositions are also diverse; therefore the real contact angle of water droplets on solid surface is different from the Young's contact angle. To better analyze the wettability of non-ideal rough surface, the apparent contact angle θ^* is introduced, and it is usually measured in the actual situations [55]. Wenzel made an assumption that liquid on the microscopic rough surface can always fill the rough structure on the non-ideal surface (see Figure 6a) [56]. Through investigating the energy change of the droplets during the wetting process on the rough surface [57], Wenzel considered that the apparent contact angle θ^* exhibits the following relationship with the Young's contact angle θ :

$$\cos \theta^* = r \cos \theta \quad (2)$$

This formula is the famous Wenzel wetting equation, where r is defined as the roughness factor, and mainly refers to the ratio of actual solid–liquid interface contact area to the apparent solid–liquid interface contact area, and obviously $r \geq 1$. Based on the Wenzel wetting equation, a series of wetting phenomena were well explained at that time. Under the hydrophilic condition ($\theta < 90^\circ$), the apparent contact angle θ^* decreases with the increase in the roughness, and the surface is more hydrophilic. In contrast, under the hydrophobic condition, the apparent contact angle θ^* increases with the increase in the roughness, and the surface exhibits higher hydrophobicity. Therefore, the Wenzel wetting

equation indicates an important theoretical direction for the design of special superhydrophobic coatings. It reveals that the microscopic rough structure can effectively control the apparent contact angle θ^* , and change the wetting performance of solid surface.

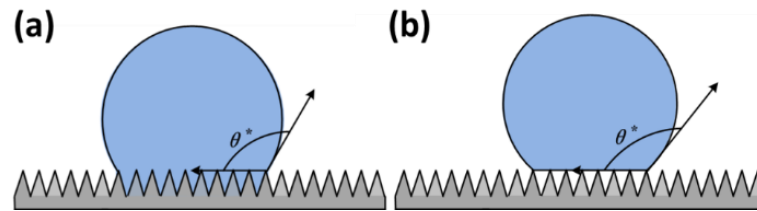


Figure 6. (a) Wenzel wetting model and (b) Cassie–Baxter wetting model.

2.3. Wetting on Non-Ideal Surfaces—Cassie–Baxter Equation

Wenzel equation well reveals the relationship between the apparent contact angle θ^* on the rough surface and Young's contact angle θ . However, it has been found that there are still many wetting phenomena in nature such as the rolling water droplets on lotus leaf surface and the rapid dropping of water from the ladybug's back cover, which cannot be explained by Wenzel equation [58–61]. Cassie and Baxter thus further expanded the Wenzel equation, and they considered that Wenzel equation was suitable for hydrophilic and partially hydrophobic materials, yet for some superhydrophobic phenomena (the apparent contact angle greater than 150° and the roll angle or contact angle hysteresis less than 10°), Wenzel equation was no longer applicable. Cassie and Baxter agreed that the contact interface between droplet and some superhydrophobic surface was not a single solid–liquid fully infiltrated contact interface. However, it was a type of composite phase contact interface of solid–liquid and gas–liquid contact interfaces which exist on the contact interface at the same time, as shown in Figure 6b. Mathematical relationship between the apparent contact angle θ^* and the Young's contact angle θ_1 and θ_2 can be given by the following equation:

$$\cos \theta^* = f_1 \cos \theta_1 + f_2 \cos \theta_2 \quad (3)$$

where θ_1 and θ_2 are the Young's contact angles of the liquid droplet on the solid and gas, respectively, f_1 and f_2 are the percent for the solid–liquid contact area and the gas–liquid contact area in apparent contact area, and $f_1 + f_2 = 1$. The Young's contact angle θ_2 can be considered to be 180° , thus Equation (3) becomes:

$$\cos \theta^* = f_1 \cos \theta_1 + f_1 - 1 \quad (4)$$

which explains some special non-wetting superhydrophobic phenomena. Some microscopic structures on the surface of hydrophobic materials can effectively entrap the air pockets underneath the liquid droplets, so that droplets cannot infiltrate into the internal microstructure. In this case, the apparent solid–liquid contact interface is actually composed of solid–liquid and gas–liquid interfaces. The smaller the proportion of actual solid–liquid contact area in apparent contact area, the higher the value of apparent contact angle θ^* is induced. The droplets are hovering on the solid surface, achieving superhydrophobicity [62–65].

2.4. Relation between Wenzel Equation and Cassie–Baxter Equation

It has been demonstrated that apparent contact angle θ^* is also insensitive to the external fields. Moreover, it is noteworthy that the use of the notion “apparent contact angle” (for Wenzel and Cassie–Baxter wetting equations) is justified on the scale much larger than the characteristic scale of the microscopic structure roughness [66]. It is reasonable to assume that the apparent contact angle on gravity measured in experiments is due to the phenomenon of the hysteresis of the contact angle.

The Young's contact angle should be defined as the angle supplying minimum to the free energy of a solid/liquid/air system.

Both Wenzel and Cassie–Baxter equations can explain the effect of surface textures on non-wettability; however, the two internal mechanisms are different. Wenzel wetting theory determines that the contact between solid and liquid is a complete infiltration form. Based on the microstructure design, the increased actual contact area of solid–liquid can effectively enhance the non-wetting ability of solid surface with a maximum apparent contact angle θ^* of $\sim 150^\circ$ [67,68]. Cassie–Baxter wetting theory holds that the special microstructure entraps a large amount of air pockets underneath liquid droplets, therefore the contact type between solid and liquid is composite contact. The actual solid–liquid contact area is significantly reduced, which leads to the increase in the apparent contact angle θ^* to 150° , or even beyond [69]. Furthermore, the difference between both the wetting models can induce more distinguishing moving characteristics of liquid droplets on the solid surfaces.

2.4.1. Contact Angle Hysteresis and Rolling Angle

Although Furmidge reported the importance of the studies on the moving characteristics of droplets on solid surfaces [70], during a long period of time the study on superhydrophobic coatings still focused on enhancement of apparent contact angle. Contact angle hysteresis reflects the motion capacity of droplets on the solid surfaces [71]. When the contact angle hysteresis is less than 10° , the droplets are easily removed away from the surface. Contact angle hysteresis $\Delta\theta$ is the difference value between the advanced contact angle θ_A and the receding contact angle θ_R . When the reference droplet volume is slowly increased until the three-phase contact line moves, the maximum apparent contact angle is called the advancing contact angle θ_A . In contrast, the minimum contact angle is called the receding contact angle θ_R .

According to the theory of Wenzel wetting equation, although the contact angle of liquid droplet can reach 150° , liquid droplet does not roll easily off the surface due to high viscosity. In this case, the contact angle hysteresis is very high. Following Cassie–Baxter wetting equation theory, the apparent contact angle of droplets can not only reach 150° , but also go beyond, and the droplets can roll freely on the solid surface with smaller contact angle hysteresis [72]. The rolling angle α is used as another parameter to characterize the droplet rolling characteristics on hydrophobic surface. The minimum inclination angle of solid surface can make the liquid begin to roll off, wherein the inclination angle is called the rolling angle. The rolling angle is related to several factors such as static contact angle, contact angle hysteresis, and droplet size [73,74]. Wolfram proposed a rolling angle equation to describe the rolling ability of droplets on solid surface [75] as follows:

$$\sin \alpha = k \frac{2\pi l}{mg} \quad (5)$$

where l is the radius of the contact area between droplet and solid surface, m is the mass of the droplet, g is the acceleration due to gravity, and k is the proportionality constant. Subsequently, Murase et al. further arranged Equation (5) to describe the relationship between the rolling angle and the contact angle [76] as follows:

$$l = R \sin \theta \quad (6)$$

$$R' = \left[\frac{1}{4} (2 - 3 \cos \theta + \cos^3 \theta) \right]^{1/3} R \quad (7)$$

$$\frac{3}{4} \pi R'^3 \rho g = mg \quad (8)$$

Equations (6)–(8) are substituted into Equation (5) to obtain the following relations:

$$k = \left[\frac{9m^2 (2 - \cos \theta + \cos^3 \theta)}{\pi^2} \right]^{1/3} \times \frac{\sin \alpha (g\rho^{1/3})}{6 \sin \theta} \quad (9)$$

where ρ is the density of droplets, R' and R are the radii of droplet, while m is the quality. Clearly, we can calculate the proportional constant k on any flat surface, and confirm that coefficient k exhibits the relationship with the interface energy between solid and liquid. Calculation of the transition energy barrier between Wenzel wetting model and Cassie–Baxter wetting model indicates that water droplets in Wenzel wetting model have higher rolling angle, while water droplets in Cassie–Baxter wetting model can easily roll with a smaller rolling angle. Thus, contact angle hysteresis bears certain relationship with the rolling angle, yet some obvious difference is accompanied. It is more meaningful to use rolling angle to describe the roll characteristics of droplets on solid surfaces, while contact angle hysteresis can well reflect the sliding or viscous characteristics of droplets on solid surface [77]. Therefore, it is of great significance to investigate the kinematic characteristics of water droplets on solid surfaces under both the wetting theories to achieve the objective of designing special function modification on solid surfaces.

2.4.2. Critical Conditions for Wetting State Transition

Dettre and Johnson [78] simulated the microstructure surface based on Wenzel equation and Cassie–Baxter equation, and found the existence of a critical value for the roughness factor of solid surfaces. Beyond this threshold, the wettability model changes from Wenzel wetting model to Cassie–Baxter wetting model. With the greater roughness factor, the more stable Cassie–Baxter wetting state with enhanced non-wettability is obtained [79]. Based on the fact that the micro–nanoscale composite structure on the surface of lotus leaf causes a high apparent contact angle and a very low contact angle hysteresis (see Figure 7), the structural effects of lotus leaf surface and the bionic preparation techniques have attracted significant attention [37,80–82], which makes the research of the intrinsic relationship between special non-wettability and microstructure to have a leap-forward development. It is well known that on a rough surface containing microscale structure, the main contact interface between droplet and solid surface is in infiltration state, and Wenzel equation theory is applicable [83]. According to the continuous optimization of single-stage structure scale (a larger aspect ratio), it is also possible to geometrically increase the apparent contact angle of droplets, which even reach 160° . When the surface has a micro–nanoscale composite structure (even if the contact interface is still in infiltration type under the condition of single microscale structures), the overall contact interface between composite structure and droplets is still a composite type, and Cassie–Baxter equation theory is applicable in this case [84]. Owing to the induction of the secondary nanostructures, the infiltration contact state of the primary structure is eliminated. Consequently, the micro–nanoscale structure surface is still in a non-infiltration contact state with a high apparent contact angle and a very low contact angle hysteresis [85–88].

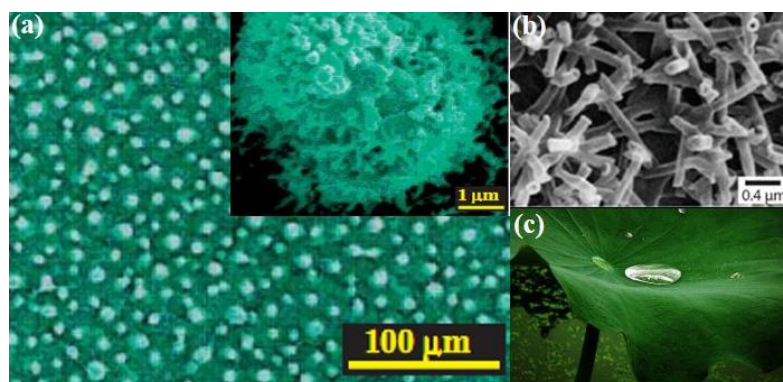


Figure 7. Micro–nanoscale composite structures of Lotus leaf surface: (a) Natural lotus leaf surface structure; (b) Biomimetic composite structure. (Reproduced from [82] with permission; Copyright 2002 Wiley). (c) The droplet on the lotus leaf surface.

Therefore, superhydrophobic surface gradually develops with the construction of microscopic structures from single-stage microscale structure to micro–nanoscale composite structure. The secondary nanostructure can easily eliminate the infiltration contact state caused by the primary microscale structure, leading to greater significance to reduce the contact angle hysteresis and guiding the direction of manufacturing microscopic structures for the ultra-hydrophobic materials [89,90].

3. Preparation Techniques of Superhydrophobic Coatings

According to the above-mentioned analyses, superhydrophobicity is mainly dependent on surface free energy and microscopic rough structures. There are following two main strategies to reduce surface free energy: one is the use of hydrophobic materials with low surface free energy as matrix materials, such as polytetrafluoroethylene (PTFE), etc. The another one is to utilize the matters with low surface free energy to modify solid materials [91,92]. The preparation of superhydrophobic coatings still focuses on the construction of suitable microscopic structures. Some current preparation techniques are discussed in detail in the following sections.

3.1. Lithography Technique

Advanced printing technologies, such as X-ray exposure technology, electron beam exposure technology, and lithography development technology are gradually applied to the construction of microstructures. Their main advantage includes the design and manufacture of regular structures on the surface of solid materials according to the experimental requirements [93]. Angelo et al. reported a type of regular structure on poly methyl methacrylate (PMMA) sheet to produce superhydrophobicity, and the photolithography and ion etching techniques were effectively applied [94]. The resultant sample surface displayed higher non-wettability with the apparent contact angle reaching 171° and contact angle hysteresis as low as 5° . Furthermore, Hee-Tak Kim group proposed a structural shape based on the vertical movement of azo-material driven by directional photofluidization imprint lithography (DPIL) [95], as shown in Figure 8. The technique provides a facile approach to fabricate complex hierarchical micro–nanostructures. By performing two-step light exposure process on a stack of the PDMS mold and prestructured PDO 3 film, a range of patterns with sizes of features from micrometers to 100 nm was successfully fabricated on a large scale. The results showed that the dual-scale micro–nanostructures exhibited excellent superhydrophobic property, and endowed with great self-cleaning function.

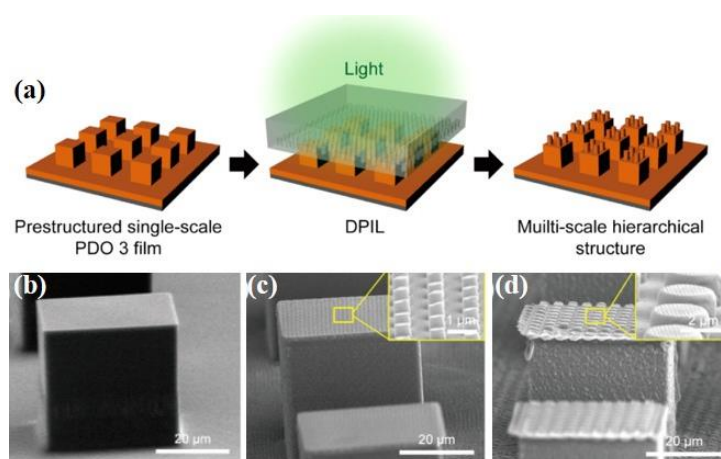


Figure 8. Hierarchical micro–nanostructures formed by DPIL: (a) Schematic illustration of the fabrication process, (b) cross-sectional SEM images of a prestructured box pattern; (c) dual-scale structure with a submicron pillar pattern on top, and (d) the triple-scale structure with a sub-100 nm line pattern on top and a micron-pillar patterns on the second level. (Reproduced from [95] with permission; Copyright 2017 American Chemical Society).

3.2. Phase Separation Technique

Phase separation technique is a low-cost method to prepare superhydrophobic coatings. In this process, the mixture containing two phases are separated into two single phases via heating or cooling at the same time to produce superhydrophobic surface with micro–nanoscale composite structures. Typically, addition of insoluble solvents into the polymer solution can provide polymer with aggregated and non-aggregated phases [96,97]. The continuous film with porous structures is produced through the chemical and physical interactions. Kato and Sato constructed a superhydrophobic coating with micro–nanoscale structure, with a higher apparent contact angle of 163° by the ultraviolet (UV)-induced phase separation technique [98]. This method significantly simplifies the preparation technology of superhydrophobic coatings, and is verified with a certain degree of universality on the transparent glass substrate and the fabric surface [99]. Xiong et al. successfully prepared breathable superhydrophobic coating by one step spraying technique and non-solvent vapor induced phase separation [100], as shown in Figure 9. The addition of inorganic silica (SiO_2) nanoparticles into the polymer solution significantly improved the superhydrophobicity and strengthened the mechanical properties after being thermally treated. It was observed that apparent contact angle on the composite coatings was greater than $160.1^\circ \pm 2.2^\circ$, when the mass ratio of with polymer to hydrophobically modified fumed silica (HMFS) nanoparticles in mixtures was 15:4. Moreover, after the acid and base treatments, apparent contact angle remained greater than 150° , which is mainly attributed to the superhydrophobicity, leading to the repulsion of aqueous media away from the coatings. Therefore, such coatings have great potential for practical applications.

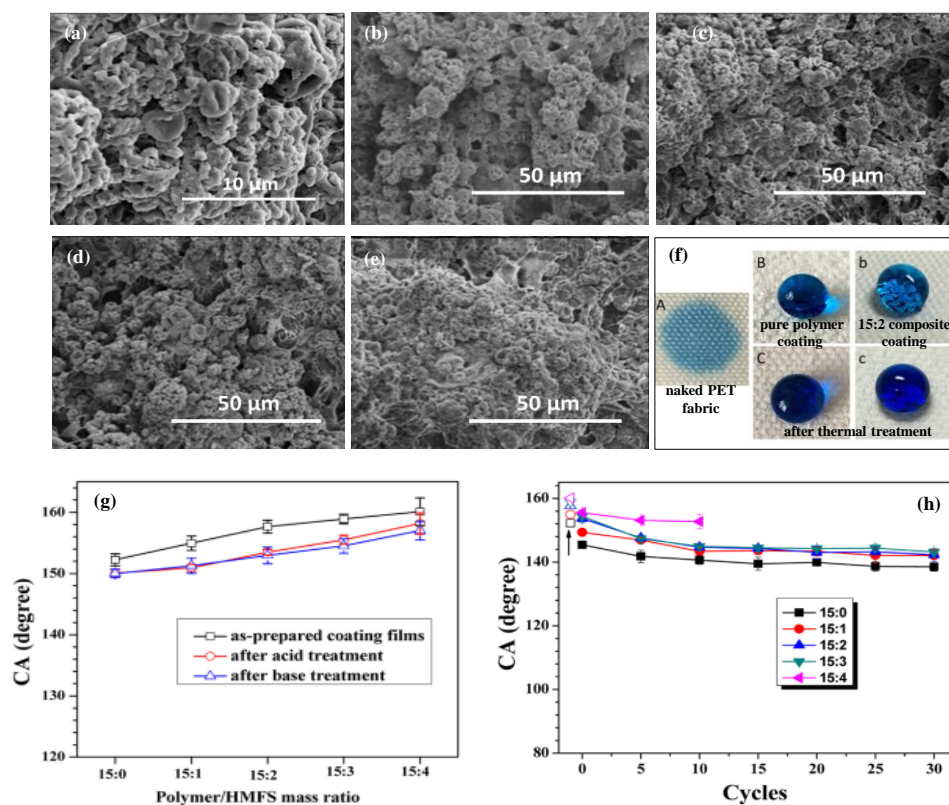


Figure 9. SEM images showing the morphologies of the superhydrophobic coatings with different mass ratio of polymer and HMFS nanoparticles: (a) 15:0, (b) 15:1, (c) 15:2, (d) 15:3, and (e) 15:4. (f) Photographs displaying ink–water droplets stably sitting on composite coatings. (g) Apparent contact angle of the composite coatings immersed in buffers with pH = 1 and 14 for 12, respectively. (h) Apparent contact angle versus the sandpaper-abrasion test cycles for the composite coatings. (Reproduced from [100] with permission; Copyright 2017 Elsevier).

3.3. Templating Processing Technique

Templating processing strategy mainly refers to the fabrication of the superhydrophobic coatings from the harden separation of the original rough structural material. This method is mainly used to copy the natural animal skin and plant leaves to design micro-textures, and then prepare the superhydrophobic coatings/surfaces [101]. Hou et al. copied the surface microstructure of a filter paper through the template processing technology and prepared superhydrophobic PTFE surface [102]. Vogel et al. used colloidal self-assembly and templating methods to create two-dimensional nanopore arrays with precisely adjustable re-entrant curvatures (Figure 10a) [103]. The simple nanoscale architecture, prepared by backfilling a colloidal monolayer with a variation of concentration of sol-gel precursor, enables us to rationally tailor the macroscopic wetting properties, even for low-surface-tension liquids (as shown in Figure 10b,c). Compared to a flat reference surface with similar surface chemical compositions, the contact angles of liquids on the surface with open structures strongly increase and exceed 100° . Figure 10f exhibits the continuous increase in the contact angle with the change of liquid surface tension from 21.7 mN m^{-1} (octane) to 72.8 mN m^{-1} (water).

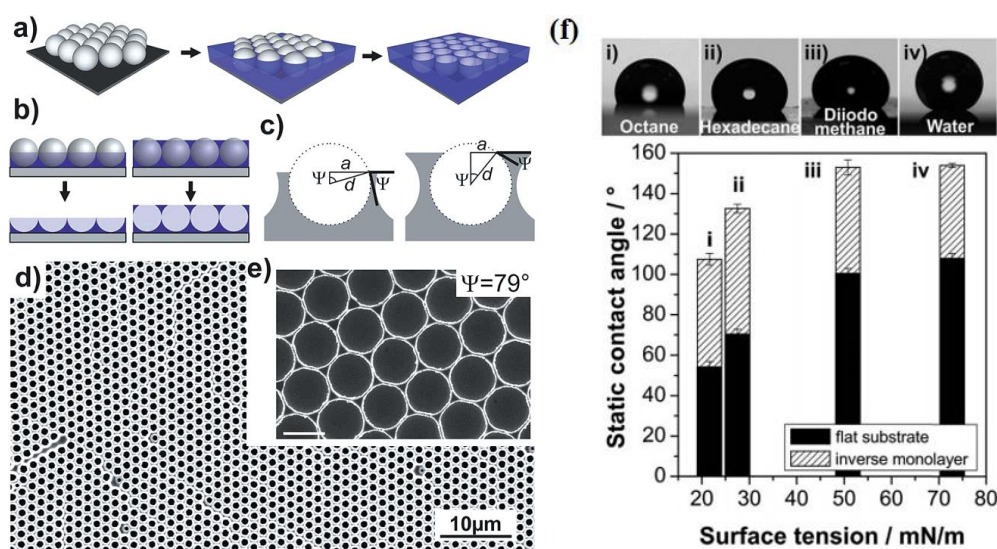


Figure 10. (a) Schematic illustration of the fabrication process of re-entrant structures from colloidal monolayer templates; (b) The precise controlling of pore opening by changing the content of SiO₂ precursor; (c) Geometric illustration of the relationship between the pore radius a , colloidal radius d , and the pore opening angle Ψ for two exemplary pore openings; (d) SEM image of the prepared nanopore arrays and the corresponding inverse monolayer with pore openings of $\Psi = 79^\circ$; and (e) Static contact angle of liquids with various surface tensions on inverse monolayers functionalized by fluorinated surface chemistry, scale bar is $1 \mu\text{m}$. (f) The continuous increase in the contact angle with the change of liquid surface tension from 21.7 mN m^{-1} to 72.8 mN m^{-1} . (Adapted from [103] with permission; Copyright 2016 RSC).

3.4. Etching Technique

Etching technique mainly refers to the method involving the use of laser, plasma, electrochemical, and chemical ways to manufacture large-area rough microstructure [104–107]. Based on the urgent requirements for metal surface modification, it is promising to use the etching method on metal surface to build micro-nanoscale structures and obtain superhydrophobicity. Wang et al. constructed the micro-nanoscale composite structures on metal surface by the combined template and plasma etching technique, and obtained a superhydrophobic surface with an apparent contact angle reaching 153° after low surface energy modification [108]. Liu's group reported an easy method to prepare superhydrophobic micro-nanostructures on brass surfaces via micro-etching technology [109], and the

surface energy was reduced via stearic acid modification (see Figure 11a). Under the micro-etching operation of 6 min, the modified sample surface exhibited the excellent superhydrophobicity with higher contact angle of 152.4° and lower slide angle of 5.3° . This was mainly attributed to more air pockets entrapped easily in the spaces between the clusters due to numerous hemispherical dandelion-like clusters with an average size of $10\ \mu\text{m}$. However, the surface required the improvement in its thermal stability for its application in strong thermal environments. Furthermore, the as-prepared sample was verified to possess an excellent self-cleaning ability, wherein the carbon dust was easily removed away from the surface under the action of rolling water drops.

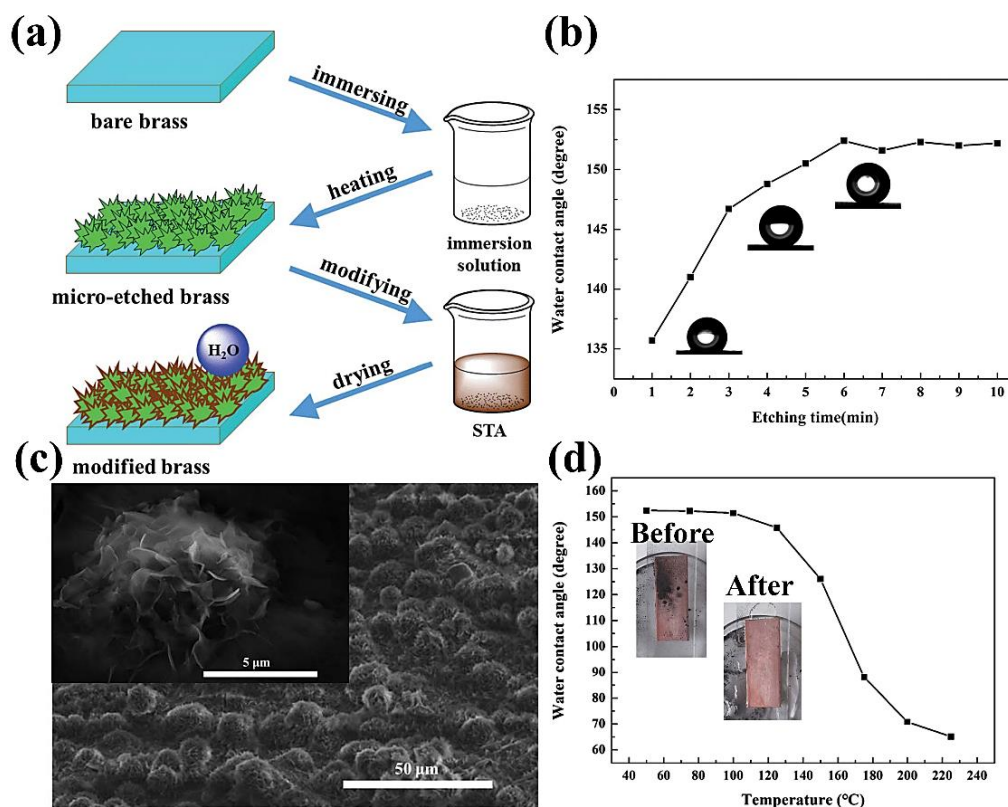


Figure 11. (a) Schematic illustration of the process of fabrication of a superhydrophobic surface on the brass substrate; (b) Effects of the micro-etching time on contact angle of the as-prepared surface; (c) SEM images of the as-prepared surfaces with micro-etching period of 6 min; and (d) Thermal stability test results for the superhydrophobic brass and self-cleaning behavior of the superhydrophobic brass surface (inset). (Adapted from [109] with permission; Copyright 2017 RSC).

3.5. Sol–Gel Technique

Sol–gel technique has been known for a long time, and it is mainly used to prepare nano-particles or nano-film materials. In recent years, sol–gel technology has also been gradually utilized for the fabrication of superhydrophobic coatings for applications in aviation and shipbuilding [110,111]. Lu et al. prepared superhydrophobic SiO_2 films on the surface of aluminum alloy by the pulling method [112], where SiO_2 nanoparticles were added into a mixture of $\text{C}_2\text{H}_{12}\text{N}_4$ and $\text{Zn}(\text{NO}_3)_2 \cdot 6\text{H}_2\text{O}$ to prepare sol. Dong and Ha fabricated superhydrophobic polysilsesquioxane/polystyrene microspheres with flower-like structures via a cetyltrimethyl ammonium bromide-assisted sol–gel approach [113]. The structure produced by nanoparticles on microcores could be controlled from raspberry- to flower-like morphology precisely through adjusting the content of silane precursor. Miraculously, owing to the hierarchical particulate films with the initial ethyl groups, hierarchical microspheres

exhibited good superhydrophobic properties without any surface modification after assembling these on glass substrates in Figure 12.

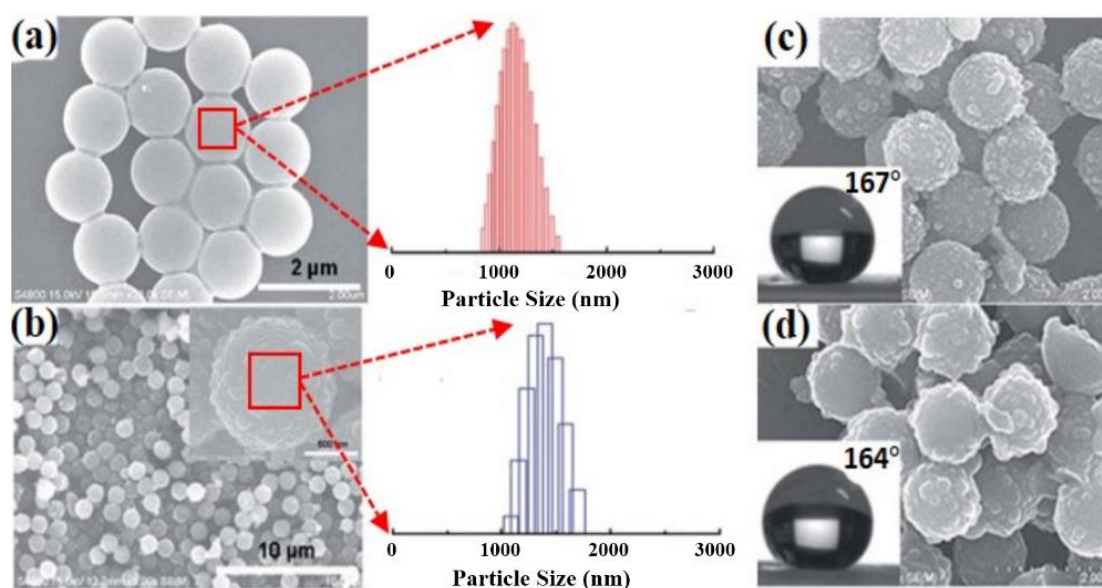


Figure 12. SEM images of the hierarchical polysilsesquioxane/polystyrene microspheres and corresponding particle size distribution: (a) SEM image of polystyrene latex beads with the corresponding particle size distribution; (b) SEM images of the hierarchical microspheres with the corresponding size distribution; and (c,d) SEM images of hierarchical polysilsesquioxane/polystyrene microspheres with different contents (3 and 7 mmol) of ethyltrimethoxysilane. (Adapted from [113] with permission; Copyright 2017 RSC).

3.6. Electrostatic Spinning Technique

Electrostatic spinning technique is a new method employed for the fabrication of superhydrophobic surface [114]. Ma et al. used electrostatic spinning technique to prepare polycaprolactone polymer layer on the substrate surface [115], and then through the chemical vapor deposition method, modified the formed microstructure to obtain superhydrophobic surface with the apparent contact angle reaching 175° and rolling angle being only 2.5° . It is noteworthy that controlling the membrane properties, such as hydrophobicity and hydrophilicity, is critical to achieve desirable macroscopic performance. During a long period, the difference in the surface wettability between superhydrophilic poly(*m*-phenylene isophthalamide) (PMIA) electrospun nanofibrous membranes (ESMs) and the superhydrophobic parent material was believed to arise from the poling effect induced by the electrospinning process. To eliminate the poling effect, Ouyang et al. prepared a PMIA ESM [116], and used a centrifugally spun nano fibrous membrane (CSM) as a reference sample. Finally, the changes of surface properties of the membranes at the molecular level were investigated. The results showed that the wettability of the ESM was very different from that of the CSM due to the presence of a large number of *cis*-amide groups on the surface resulting from the conformational changes, as shown in Figure 13. Clearly, the *cis*-amide conformation significantly enhances the electrostatic attraction between the ESM and cations, thus increasing the adsorption capacity of the membrane for the dye molecules and enhancing the *in situ* growth of metal nanoparticles.

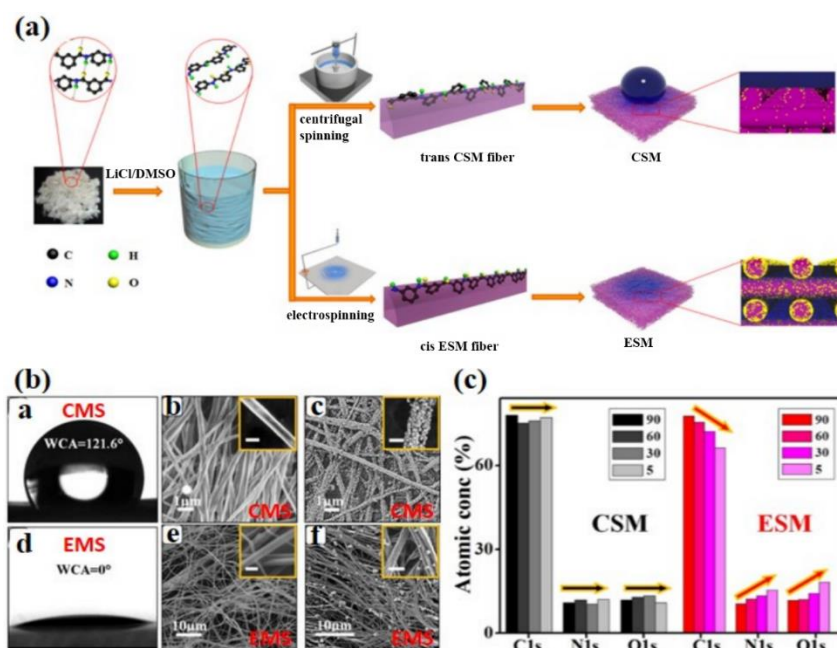


Figure 13. (a) Schematic illustration of the formation of the cis-PMIA ESM; (b) Static contact angles of water droplets on the PMIA CSM and PMIA ESM and representative SEM images of nanofibers on the PMIA CSM/Pt and PMIA ESM at Pt precursor concentrations of 0.01 M; and (c) ARXPS spectra of the CSM and ESM at different test depths. (Adapted from [116] with permission; Copyright 2017 ACS).

3.7. Other Methods of Preparation

Preparation of superhydrophobic coatings mainly depends on the microscopic structures which can also be constructed by methods other than described above, such as self-assembly method, alternating deposition method, and particle filling method [117–121]. Yamauchi et al. sprayed the polyvinylidene fluoride solution with PTFE nanoparticles onto plastic substrate to obtain the superhydrophobic coatings with the apparent contact angle reaching 150° [122]. Soeno et al. deposited the wafers alternately in a mixed solution of polyallylamine hydrochloride and polyacrylic acid containing SiO_2 nanoparticles to obtain a multilayer assembly film [123]. After the heat treatment, the electrolyte in the membrane was removed and the SiO_2 nanoparticle membrane with composite structures was obtained which exhibited higher superhydrophobicity (apparent contact angle of $\sim 166^\circ$).

Currently, the huge application prospects of superhydrophobic coatings are gradually gaining significant attention, and many preparation techniques have been developed [124]. As a response, the superhydrophobic coatings are expected to bring technical innovations to human daily life, industrial production, and aerospace technology, etc.

4. Dynamic Water Repellency

In general, most of the superhydrophobic surfaces have a static water contact angle greater than 150° and demonstrate wetting properties similar to those of lotus leaves. However, they may not really behave exactly like lotus leaves when dynamic water droplets impact them. Therefore, the impingement of water droplet has also been investigated to characterize the wettability of superhydrophobic coatings under dynamic conditions [125]. Currently, bouncing dynamics of impact droplets on solid surfaces intensively appeal to researchers due to its importance in many industrial fields, including anti-icing, dropwise condensation, and self-cleaning. The impact of droplets on a solid surface is followed by spreading, recoiling, and bouncing off. It has also been demonstrated that the bouncing dynamics are highly dependent on surface texture and wettability, and also on the properties of the droplet (i.e., impact viscosity, surface tension, density, and radius) [126,127].

Based on these characteristics, many researchers utilized the synergistic actions of surface chemical compositions and microstructures to construct the hydrophobic or superhydrophobic surface for rapid drop detachment [128–131].

The process of droplets impacting on a solid surface is a key phenomenon in a variety of natural and industrial fields. When a droplet impacts a superhydrophobic surface, the air trapped between droplet and rough structures offers a considerable capillary pressure that helps in rebounding of the droplet off the surface [132–134]. In contrast, when a droplet impinges on a hydrophilic or hydrophobic surface, it tends to wet the surface by either spreading on or sticking onto the surface. Li et al. investigated the dynamic processes involving the impact of water droplet on flat, porous, and pincushion structured films [135]. The results revealed that rebound characteristics were governed by the energy dissipation during the impact and wetting transition within the structure. Yong et al. performed water droplet impact dynamics and underwater stability studies using ZnO/Si hierarchical nanostructures (HNs) as a model system [136] in Figure 14. Results indicated that decrease in the Weber (We) number could induce the conversion of the wetting state to the anti-wetting state because of the decrease in relative magnitude of wetting force compared to the surface energy. This could be attributed to the fact that two downward pressures and one upward pressure jointly affected the movement of the water droplet during the impacting process [137–139]. The two downward pressures (wetting pressure and effective water hammer pressure) are forces that penetrate the micro/nanostructure's air pockets. However, the upward pressure (capillary pressure) is a force that interrupts the penetration of the water droplet. When the sum of the downward pressures is greater than the upward pressure, wetting is observed in the water droplet impacting the surface.

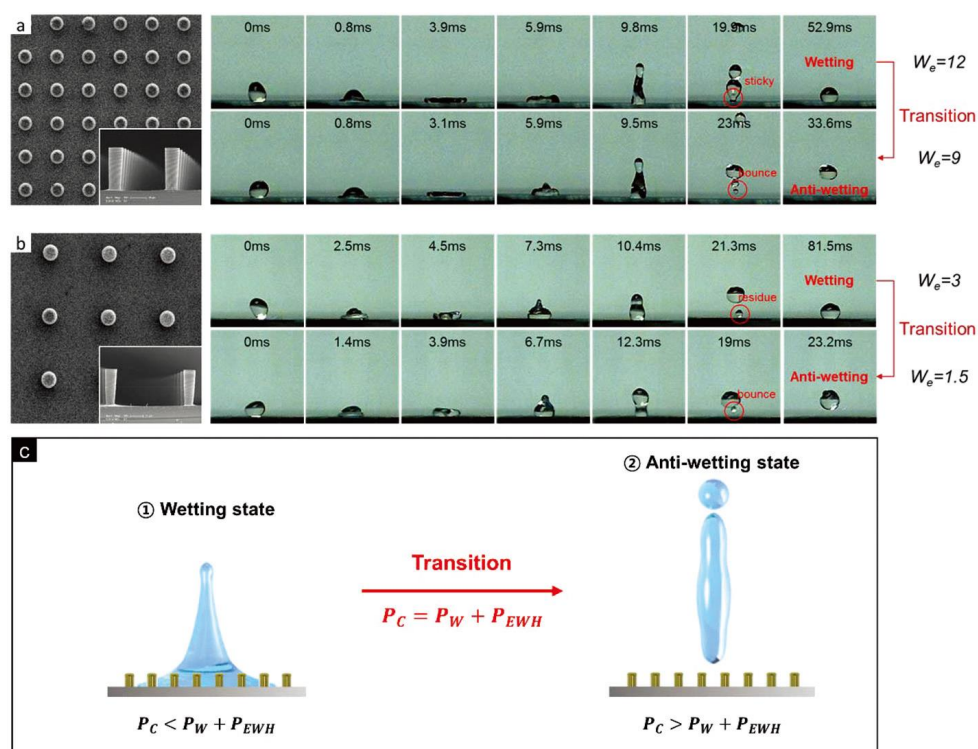


Figure 14. Snapshots of the impact dynamics of water droplets showing the transition between wetting/anti-wetting states at a critical We number: (a) ZnO/Si HNs with 50 μm spacing distance, showing a transition from the wetting state to the anti-wetting state at $We = 9$; (b) ZnO/Si HNs with 100 μm spacing distance, showing a transition from the wetting state to the anti-wetting state at $We = 1.5$; and (c) Schematic representation describing the transition from the wetting state to the anti-wetting state. (Adapted from [136] with permission; Copyright 2017 RSC).

Moreover, our group has also reported several literatures on water droplets impacting an extremely hydrophobic surface. To reduce the contact time between the impacting water droplet and the superhydrophobic surface, we reported an ultra-water-repellent surface with the ternary composite structures (macro ridge, microscale patterns, and nanowire structures), and further probed the capacity to compel the impacting water droplet to bounce off within an extreme short time, as shown in Figure 15a,b [140]. Based on this, we found that droplets impacting onto dome convex surfaces could also rapidly bounce off with the contact time decreasing to 8.0 ms (see Figure 15c). Although the reduction in contact time of impact droplets was not extremely remarkable compared to that of the above mentioned macroscopically flat surfaces, the convexity was induced to produce a distinguishing bouncing regime. The convexity could expedite the movement of impact droplets on solid surfaces. Furthermore, the underlying physics revealed that the convexity could induce the impact droplet to produce an upward inertia force perpendicular to the convex surface during the retracting process, which was also powerfully propped up by the quantitative numerical calculation results (Figure 15d). The presented research will broaden the understanding on the regime behind some wetting phenomena [141].

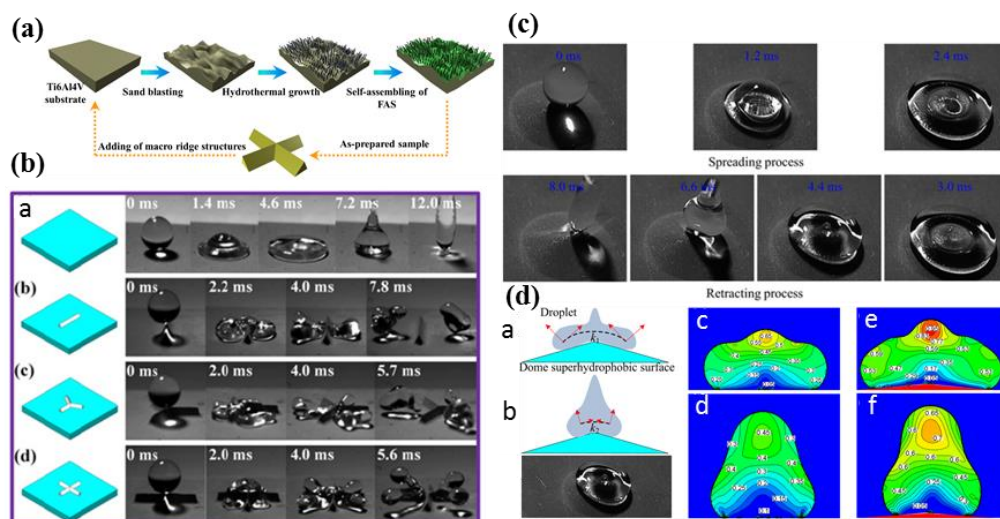


Figure 15. (a) The schematic illustration of the fabrication of the ultra-water-repellent surface; (b) The macro ridge structures on the as-prepared superhydrophobic surface, and the corresponding contact processes of the impact water droplet [140] (copyright © 2016 Elsevier B.V.); (c) The moving process of the impact droplet at $We = 6.87$ until bouncing off the convex superhydrophobic surface; and (d) The schematic illustration of forced direction variation from stage k1 to stage k2 during the retracting process (a,b). The numerical results of impact droplet retracting at the two particular moments on the flat (c,d) and dome convex (e,f) surfaces. (Adapted from [141] with permission; Copyright 2016 AIP).

5. Anti-Icing Application

5.1. Anti-Icing Theory

Fabrication of high-performance anti-icing materials is still a worldwide technical challenge. Although no material can completely resist the ice accumulation, in recent years, scientists continued to analyze the process of ice formation and accumulation. They found that some appropriate surface modification techniques can make the substrate materials to be endowed with superhydrophobicity and the ability of reducing ice adhesion [142–148]. According to the previous analyses of wetting theory, key factors for obtaining superhydrophobicity are lower surface free energy and microscopic rough structures. It has been found that such a rough structure can not only effectively increase the surface superhydrophobicity, but also produce some anti-icing performance under certain conditions [149].

Anti-icing is a complex phenomenon that requires a multi-disciplinary approach in research. Broadly speaking, the problem can be investigated around three major aspects. First is the interaction between water and the solid surface. In a practical situation, if a water droplet is able to slide off or removed from the surface before freezing, ice will not be formed on the surface. The second area of focus is icing delay, in terms of delay in either time or temperature. A lower ice formation temperature would enable a wider operating window in temperature, and thus a higher productivity and economic return. Similarly, a longer freezing time would increase the chance of water removal before the formation of ice. The third, or the last defense line, is the ice adhesion. When ice inevitably forms, the ice adhesion should be kept as weak as possible in order to easily remove the ice by applying a small external force or even by the centrifugal force of a moving component (e.g., wind turbine blade). The detailed contents are discussed as follows:

Superhydrophobic surface with microscopic rough structure is conducive to capture air pockets underneath the droplets to form Cassie–Baxter wetting model. At the same time, the air becomes a good thermal insulation layer to prevent droplets from freezing, thus achieving the purpose of delaying icing [150–154]. Cao et al. added nanoparticles into polymer composite substrates and obtained the superhydrophobic surface [155]. Metya et al. investigated the ice nucleation of a supercooled cylindrical water droplet on nanotextured surfaces at 203 K with the Cassie–Baxter and Wenzel states using molecular dynamics simulations [156], as shown in Figure 16. On the one hand, ice nucleation rate was found to enhance with the increase in surface fraction in the Cassie–Baxter state, whereas the nucleation rate decreased for the Wenzel state with increasing surface fraction. On the other hand, the effect of nanopillar height on ice nucleation was observed, indicating that the rate enhanced with increasing pillar height. Moreover, the ice adhesion was found to be significantly higher for the Wenzel state compared to that for the Cassie–Baxter state. The results presented in this study shed light on the effect of wetting states, surface fraction, and pillar height on the ice nucleation behavior on nanotextured surfaces [157].

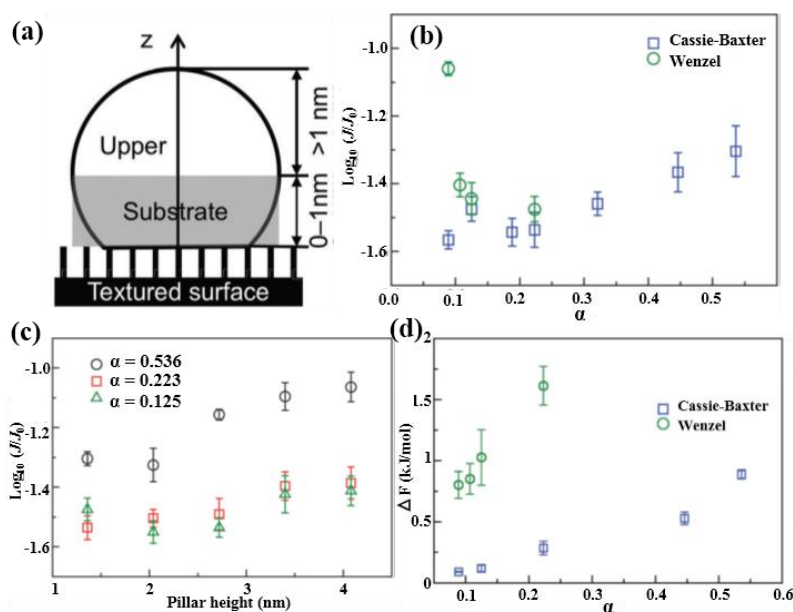


Figure 16. (a) Schematic illustration of the substrate (shaded part) and the upper region, which are 0.0–1.0 nm and greater than 1.0 nm above the surface, respectively; (b) The ice nucleation rate as a function of surface fraction at 203 K, for different nanostructured surfaces with pillar height, $h = 0.136$ nm; (c) The ice nucleation rate as a function of pillar height at 203 K, for the Cassie–Baxter state with different surface fractions; (d) Variation of the surface free energy difference with respect to α for nanostructured surfaces with different wetting states. (Adapted from [156] with permission; Copyright 2016 RSC).

Ice adhesion on superhydrophobic surface gets significantly reduced [158,159]. Researches have shown that the adhesion of ice layer on superhydrophobic surface is related to non-wettability, i.e., the value $(1 + \cos\theta_R)$ [160,161]. More precisely, the receding angle θ_R of the droplet on the solid surface exceeds 118.2° , which leads to a distinct reduction in ice layer adhesion. Therefore, the superhydrophobic surface with appropriate rough microstructure can effectively reduce the ice adhesion [162,163]. At the same time, due to a large amount of trapped air pockets, Cassie–Baxter wetting model caused by surface microstructure is effectively retained in the freezing process, thus reducing the ice adhesion [164–166]. Such a superhydrophobic surface has been proved to be effective in resisting freezing rain and fog to condense. Many achievements toward freezing process and ice adhesion have been made by us. In one of our study, we constructed hierarchical superhydrophobic surfaces by a combination of sand blasting and hydrothermal treatment on the surfaces of Ti6Al4V alloy, which displayed excellent non-wettability with apparent contact angle of 161° and sliding angle of 3° (as shown in Figure 17) [167]. Micro–nanostructures trapped a large amount of air pockets under the droplet; therefore, the icing-delay time of a droplet on the superhydrophobic surfaces was many times longer than that of a droplet on the smooth Ti6Al4V substrate, and the ice adhesion also exhibited the similar change trend.

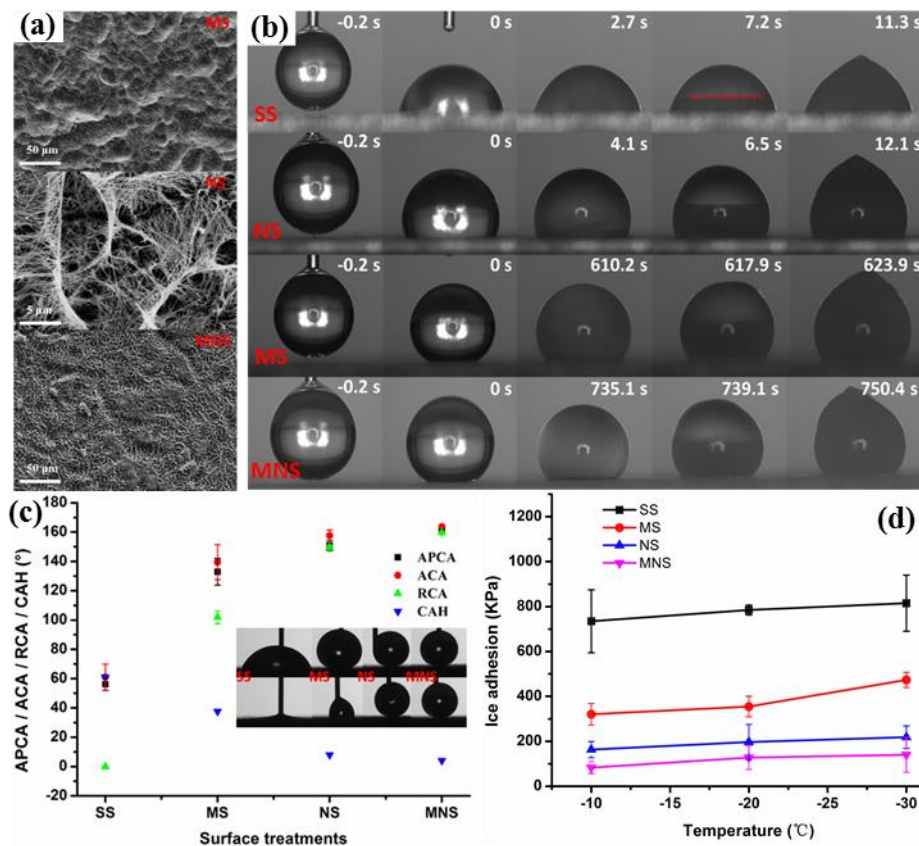


Figure 17. (a) Images of hierarchical morphologies and characterization results of the wettability of SS, MS, NS, and MNS; (b) Optical images show the icing process of 4 μL water droplets on SS, MS, NS, and MNS at -10°C ; (c) APCA, ACA, RCA, and CAH of water droplets on SS, MS, NS, and MNS; and (d) The relationship between ice adhesion strength and temperature [167]. (Adapted from [167] with permission; Copyright 2015 RSC).

Structural interface contact mechanism: Studies have shown that the air layer captured by superhydrophobic surfaces (Cassie–Baxter wetting model) is effectively retained after the droplets freeze, resulting in a high stress concentration around the bubble (acting as a microcrack). This reduces

the required external force for deicing, and the required external force is related to the retraction contact angle and the size of the voids [168]. Thus, a lower external force is required to remove the ice layer present on the superhydrophobic surface.

To further reduce the ice adhesion, Cohen and McKinley designed self-lubricating icephobic coatings with low ice adhesion strength values (~ 50 kPa) (see Figure 18a,b) [169]. Different molecular mechanisms are found to be responsible for the low ice adhesion strength, for example, the increased thickness (D) of the water depletion layer leads to the weakening of the Van der Waals interactions between the ice and the polymeric substrate. Moreover, the non-frozen quasiliquid-layer on a PDMS+PDMS-PEG surface lubricates the contact and reduces the adhesion strength between ice and solid surface. Furthermore, Gupta et al. combined the strengths of individual characteristics for low ice adhesion based on elasticity, superhydrophobicity, and slippery liquid-infused porous surfaces for an optimal combination of high water repellency and icephobicity [170]. Studies showed that an infusion of silicone oil (below 8 wt.%) with viscosity at 100 cSt in PDMS solution was sufficient to reduce the ice shear strength to an average value of 38 kPa. This ice adhesion value exhibited a $\sim 95\%$ reduction compared to a bare aluminum surface and $\sim 30\%$ reduction compared to a microtextured superhydrophobic PDMS material without oil infusion, as shown in Figure 18c,d. In general, researchers have been exploring the interface model to analyze the adhesion reduction between ice layer and superhydrophobic surface. The main objective is to generate a model with general applicability to microstructured superhydrophobic surfaces.

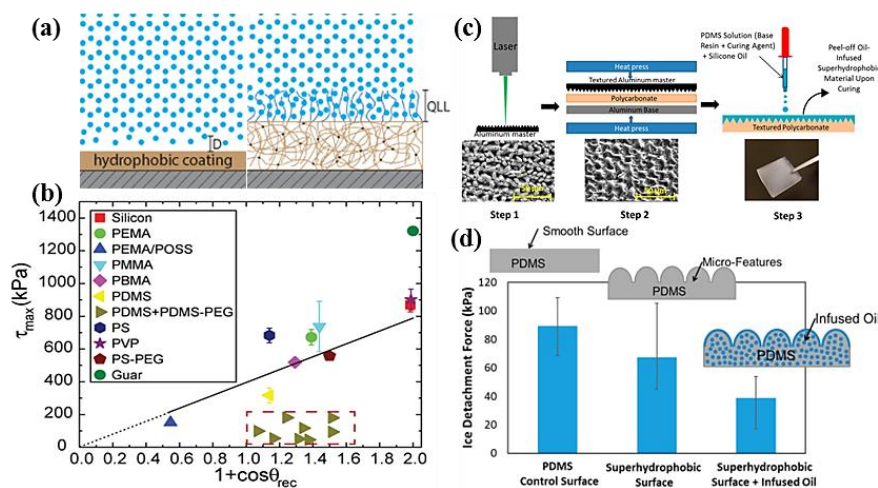


Figure 18. (a) Proposed mechanisms responsible for low ice adhesion on two distinct types of surfaces; (b) Ice adhesion strength plotted as a function of the water contact angle parameter that scales with the practical work of adhesion for water for different polymer coatings and a bare clean silicon wafer [169]. (Reproduced with permission; Copyright 2017 ACS). (c) Schematic illustration of the steps of fabrication of the oil-infused microtextured PDMS material; and (d) A comparison of ice-adhesion strength of the smooth PDMS control material, microtextured PDMS material without oil infusion, and an oil-infused microtextured superhydrophobic elastomer [170]. (Reproduced with permission; Copyright 2016 ACS).

Interface contact model and the mechanism involving the reduction of the ice adhesion on the superhydrophobic surface are complex physical and chemical processes. Although some progress has been made in this field, it is not possible to describe the mechanism of lower ice adhesion on superhydrophobic surface completely and accurately. So far, still some controversies are encountered whether the superhydrophobic surface can reduce the ice adhesion. Therefore, extensive research efforts are required to be devoted to the understanding of the basic theory about the anti-icing properties of superhydrophobic surface. Undeniably, a lot more systematic investigations are demanded to explore a more reasonable interface contact mechanism, finally providing the theoretical support for the practical applications of superhydrophobic anti-icing coatings.

5.2. Anti-Icing Property

Anti-icing property is usually evaluated around the following two aspects: icing-delay time and ice adhesion strength. The freezing process is usually observed using a camera equipped with charge-coupled device (CCD). Moreover, the icing-delay time of water droplets on the sample surfaces could be directly obtained using the CCD camera. Measurement of ice adhesion strength was performed using a self-made ice adhesion strength measurement device including a cooling plate with temperature in the range from 0 to -40 °C. To measure the ice adhesion strength, first a cuvette was filled with distilled water and sample was placed on the rabbit of the cuvette. This setup was kept in a refrigerator for more than 24 h to form an ice column sticking to the sample surface. A force transducer was used for real time monitoring of the force of separating the ice column from sample surfaces. Ice adhesion strength was calculated by using the following equation: $\tau = F/A$, where τ is ice adhesion strength; F is the critical force; and A is the contact area of ice column with sample surface.

Ruan et al. used FeCl_3 and HCl mixed solution as etchant to prepare the ideal superhydrophobic surface on the aluminum alloy matrix (apparent contact angle reached 159.1° and contact angle hysteresis was as low as 4.0°) [171]. Moreover, the anti-icing performance of superhydrophobic surface was found to be excellent. Compared to the smooth aluminum alloy matrix, the icing-delay time reached 270 s (at -10 °C) and the icing temperature dropped from -2.2 to -6.1 °C. Furthermore, other research groups have also confirmed that the anodized superhydrophobic aluminum alloy material exhibits the same excellent anti-icing performance [172].

Huang et al. etched the copper foil in the KOH and $\text{K}_2\text{S}_2\text{O}_8$ mixed solution to form a macular micro-nanoscale composite structure [173], and then modified the surface with fluorosilane to obtain superhydrophobic surface. Apparent contact angle for such surface reached 156.2° , showing a strong superhydrophobic capacity for small droplet (tens of microns). Lu et al. demonstrated the ability to spatially control frost formation and the confinement of ice growing kinetics by manipulating the free energy barrier of nucleation on the V-shaped microgroove patterned surfaces (as shown in Figure 19) [174]. Moreover, the growth kinetics of ice could also be altered by adjusting the shape of the microgroove. Ice stacked along the direction of the V-shaped microgroove (VMG), whereas it grew in random directions on the trapezoid-shaped microgroove (TMG). The insight of this study can improve the anti-icing and de-icing performances at a very cold temperature in many industrial systems.

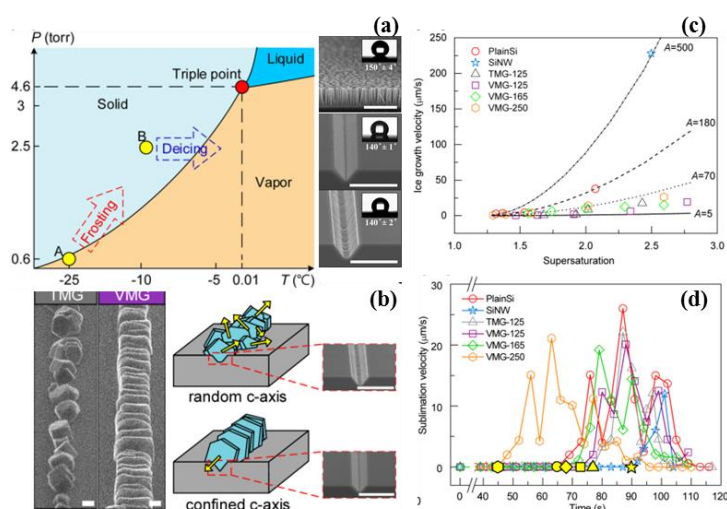


Figure 19. (a) Initial thermodynamic states of the frosting/de-icing processes and surface characterization; (b) Random and aligned orientations of c-axes on TMG and VMG surfaces, respectively; (c) Dynamics of the frosting processes under a high supersaturation condition; and (d) Dynamics of the de-icing processes. (Adapted from [174] with permission; Copyright 2017 ACS).

It is noteworthy that Aizenberg research group at Harvard University directly infiltrated the super-lubricating liquid (which is incompatible with water) into the superhydrophobic surface with porous structure, and made the lubricating liquid locked by porous micro–nanoscale composite structure, resulting in the formation of a pure liquid lubricating layer on the solid surface (see Figure 20a). Compared to conventional materials, although the apparent contact angle did not meet the superhydrophobic requirements of contact angle $>150^\circ$, the ice adhesion on the surface was reduced by 1–2 orders of magnitude because of its extreme lubricating properties [175].

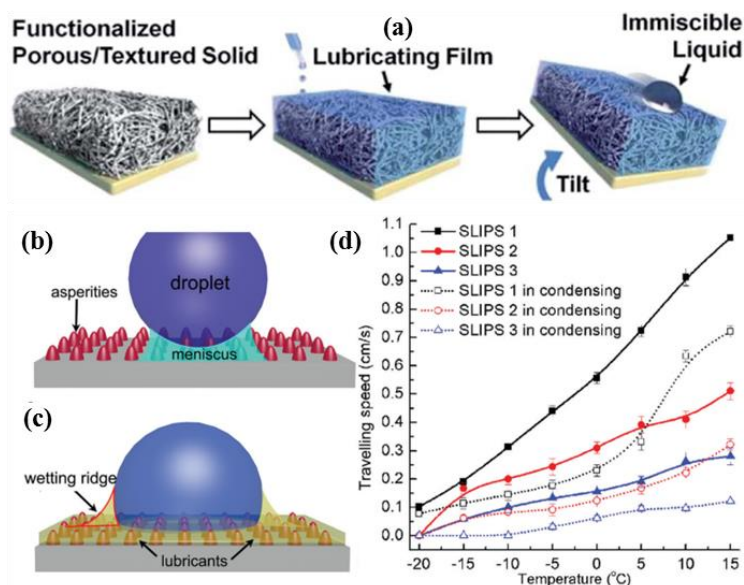


Figure 20. (a) Schematic illustration of the ultra-lubricating surface preparation process for porous materials [175]. (Reproduced with permission; Copyright 2012 ACS). Schematic representation of water droplets on the (b) superhydrophobic surfaces and (c) slippery liquid-infused porous surfaces at low temperatures. (d) Travelling speed of water droplets on slippery liquid-infused porous surfaces 1–3 versus temperature under “dry” and “wet/condensing” conditions. The surface was tilted at 3° [176]. (Reproduced with permission; Copyright 2017 RSC).

To overcome the problem of pinning up of water droplets on the prepared superhydrophobic surfaces at low temperatures due to ice/water capillary bridges, Wang et al. prepared slippery liquid-infused porous surfaces by infusing different lubricants into the superhydrophobic surfaces [176], and the water droplets smoothly travelled under the conditions of low temperatures. The results indicated superior anti-icing properties with the lower travelling speed of water droplets under the conditions of favoring the condensation of atmospheric humidity, as shown in Figure 20b–d.

5.3. Some Issues Related to Superhydrophobic Anti-Icing Coatings

Based on the above mentioned analyses, it is believed that since the discovery of fractal roughness structure in the 1990s, there have been a significant development in the theoretical research and preparation technology of superhydrophobic coatings. Moreover, the proposed theoretical model can well explain the phenomena encountered in the research process. However, the energy change and size effect in the model transition process of hydrophobic surface, in particular, for the wetting model transition mechanism led by nanostructures, still lack more detailed studies [177–180]. Second, the anti-icing application of superhydrophobic coatings is still in the basic performance evaluation stage, and the research progress also focuses on the discussion and analysis of the laboratory-based results. The studies on the anti-icing mechanism of superhydrophobic surface, in particular, the theoretical calculation and the thermodynamics and dynamic analysis toward inhibiting droplet icing nucleation growth process are still rare [181,182]. Moreover, the anti-icing research ideas about

the superhydrophobic surface also concentrate on the problem of the static droplets delaying icing and reducing the ice adhesion. However, the researches still lack the investigation of the anti-icing process for dynamic droplets, especially on energy conversion and contact time of bouncing droplets on the superhydrophobic surface [183].

Finally, the superhydrophobic surface shows a certain degree of anti-icing performance, and the current researches only hope to build the ideal non-wetting surface to solve the problem of solid surface icing. However, at lower temperatures (around $-50\text{ }^{\circ}\text{C}$), ice layer still accumulates on the superhydrophobic surface. In this case, the anti-icing application of superhydrophobic coatings still requires the coupling with the de-icing technologies, expecting to really solve the icing issues.

6. Summary and Outlook

Aircraft icing poses an increasingly serious threat to flight safety due to the damaged aerodynamic shape. The undesired ice accumulations cause a series of serious flight problems, including the redistribution of airfoil pressure, reduction of lift factor, increase in resistance coefficient, and rapid diminution of the lift resistance ratio. Moreover, it has also been confirmed that aircraft icing is mainly caused by the ice crystals and supercooled water droplets suspended in the clouds, and the formed ice generally corresponds to clear ice, rime ice, or mixed ice. Currently, the main strategy to solve the problem of aircraft icing is still based on some traditional methods such as mechanical, electrothermal, and liquid hybrid approaches, finally causing higher energy consumption and serious damage to fatigue property of substrate materials. However, considering the process of ice formation on the surface of aircrafts, the passive anti-icing coatings endowed with robust water repellency have been proposed and expected to reduce the relied degree on the traditional de-icing strategies, even replace them in near future, and finally realize the aim of fuel economy.

Superhydrophobic coating is considered to be an ideal candidate material because of its excellent water repellency, compared to the other materials such as hydrophilic materials and swelling functionalizations. Based on the surface wetting theory, the coatings decorated with the hierarchical micro–nanostructures and low surface free energy can well conform to the wetting regime of Cassie–Baxter wetting model. Moreover, the resultant surface exhibits higher contact angle and lower droplet adhesion. These theoretical analyses provide a detailed guidance on the preparation of superhydrophobic coatings. Combining with the application background, the as-prepared coatings should have a strong resistance to the mechanical damage, which is the main application challenge of superhydrophobic anti-icing coatings. Through the wide investigations on anti-icing performances of superhydrophobic coatings, the water repellency can compel the supercooled water droplets to remove off rapidly from the substrate surface before completely freezing. Even if some supercooled water droplets still manage to freeze and adhere to the substrate surface, the special wetting regime will induce smaller composite contact interface of solid/ice and air/ice, finally causing lower ice adhesion. Consequently, the ice can also be removed with the assistance of high-speed airflow around the surface of aircraft, realizing the objective of preventing ice accumulation.

Anti-icing application of superhydrophobic coatings is still in the basic performance evaluation stage, and the research progress also focuses on the discussion and analysis of the experimental results. However, it lacks the detailed study on the anti-icing mechanism of superhydrophobic coatings, in particular, the theoretical calculation and thermodynamic analysis. Nonetheless, some researchers still doubt the anti-icing potential of superhydrophobic coatings due to some complex application environments [184,185]. They consider that the microscopic structures on the superhydrophobic coatings can lead to the anchoring action with the attached ice, resulting in higher ice adhesion [186,187]. Furthermore, the anti-icing research on the superhydrophobic coatings still concentrates on the problems such as the icing-delay time of static droplets and ice adhesion, thus lacking investigations on anti-icing process of dynamic supercooled droplets (e.g., icing wind tunnel). Finally, although the superhydrophobic coatings show a certain degree of anti-icing potential, the current researches only hope to build the ideal non-wetting surface to prevent ice formation and accumulation. Freezing is a

spontaneous process, and the ice adheres to the surface of substrate materials at lower temperatures (below $-40\text{ }^{\circ}\text{C}$). Therefore, current effective strategy still requires a design of a combined approach of active de-icing and passive anti-icing with lower energy consumption in order to overcome the issue of aircraft icing.

Author Contributions: H.C. designed the setup and wrote the Sections 4 and 5. Y.L. wrote the other sections and collected the related materials. H.C., G.W., and A.L. contributed to the literatures analysis and provided the necessary assistance to Y.L.

Funding: This work was supported by the Foundation of Huaian Science and Technology Project (No. HAG201601 and HAC201705), Achievements Transformation Foundation of Huaiyin Institute of Technology (No. Z431J17506), the Project Funded by China Postdoctoral Science Foundation (2017M610329), the Natural Science Foundation of Jiangsu Province (No. BK20170790), Jiangsu Planned Projects for Postdoctoral Research Funds (No. 1701200B), and General Project of Zhejiang Provincial Department of Education (Y201737320).

Conflicts of Interest: The authors declare no conflict of interest.

References

1. Plummer, D.M.; Göke, S.; Rauber, R.M.; Girolamo, L.D. Discrimination of mixed-versus ice-phase clouds using dual-polarization radar with application to detection of aircraft icing regions. *J. Appl. Meteorol. Clim.* **2010**, *49*, 920–936. [[CrossRef](#)]
2. Cancilla, D.A.; Anke, H.; Luca, M.; Fang, X. Isolation and characterization of Microtox[®]-active components from aircraft de-icing/anti-icing fluids. *Environ. Toxicol. Chem.* **1997**, *16*, 430–434. [[CrossRef](#)]
3. Ellrod, G.P.; Bailey, A.A. Assessment of aircraft icing potential and maximum icing altitude from geostationary meteorological satellite data. *Weather Forecast.* **2007**, *22*, 160–174. [[CrossRef](#)]
4. Whalen, E.A.; Bragg, M.B. Aircraft characterization in icing using flight test data. *J. Aircr.* **2005**, *42*, 792–794. [[CrossRef](#)]
5. Jung, S.K.; Lee, C.H.; Shin, S.M.; Myong, R.S.; Cho, T.H.; Jeong, H.H.; Jung, J.H. An investigation of icing effects on the aerodynamic characteristics of KC100 aircraft. *J. Korean Chem. Soc.* **2010**, *38*, 530–536.
6. Ansell, P.J.; Bragg, M.B.; Kerho, M.F. Stall warning using flap hinge moment measurements. *J. Aircr.* **2011**, *48*, 1822–1824. [[CrossRef](#)]
7. Veres, J.P.; Jorgenson, P.C.E. Modeling commercial turbofan engine icing risk with ice crystal ingestion. *AIAA* **2013**, *2679*, 24–25.
8. Gent, R.W.; Dart, N.P.; Cansdale, J.T. Aircraft icing. *Philos. Trans. R. Soc.* **2000**, *358*, 2873–2911. [[CrossRef](#)]
9. Sabeh, Y.; Narasiah, K.S. Degradation rate of aircraft deicing fluid in a sequential biological reactor. *Water Sci. Technol.* **1992**, *26*, 2061–2064. [[CrossRef](#)]
10. Cao, Y.; Huang, J.; Yin, J. Numerical simulation of three-dimensional ice accretion on an aircraft wing. *Int. J. Heat Mass Transf.* **2016**, *92*, 34–54. [[CrossRef](#)]
11. Cober, S.G.; Isaac, G.A.; Strapp, J.W. Characterizations of aircraft icing environments that include supercooled large drops. *J. Appl. Meteorol. Climatol.* **2001**, *40*, 1984–2002. [[CrossRef](#)]
12. Smith, R.S.; Kay, B.D. The existence of supercooled liquid water at 150K. *Nature* **1999**, *398*, 788–791. [[CrossRef](#)]
13. Li, X.; Bai, J.; Hua, J.; Wang, K.; Yang, Z. A spongy icing model for aircraft icing. *Chin. J. Aeronaut.* **2014**, *27*, 40–51. [[CrossRef](#)]
14. Politovich, M.K. Aircraft icing caused by large supercooled droplets. *J. Appl. Meteorol.* **1989**, *28*, 856–868. [[CrossRef](#)]
15. Vivekanandan, J.; Zhang, G.; Politovich, M.K. An assessment of droplet size and liquid water content derived from dual-wavelength radar measurements to the application of aircraft icing detection. *J. Atmos. Ocean. Technol.* **2001**, *18*, 1787–1798. [[CrossRef](#)]
16. Westbrook, C.D.; Heymsfield, A.J. Ice crystals growing from vapor in supercooled clouds between -2.5° and $-22\text{ }^{\circ}\text{C}$: Testing current parameterization methods using laboratory data. *J. Atmos. Sci.* **2011**, *68*, 2416–2429. [[CrossRef](#)]
17. Cantrell, W.; Heymsfield, A. Production of ice in tropospheric clouds: A review. *Bull. Am. Meteorol. Soc.* **2005**, *86*, 795–807. [[CrossRef](#)]
18. Jung, S.K.; Shin, S.; Myong, R.S.; Cho, T.H. An efficient CFD-based method for aircraft icing simulation using a reduced order model. *J. Mech. Sci. Technol.* **2011**, *25*, 703–711. [[CrossRef](#)]

19. Cavalieri, D.J.; Markus, T.; Hall, D.K.; Gasiewski, A.J.; Klein, M.; Ivanoff, A. Assessment of EOS aqua AMSR-E arctic sea ice concentrations using landsat-7 and airborne microwave imagery. *IEEE Trans. Geosci. Remote Sens.* **2006**, *44*, 3057–3069. [[CrossRef](#)]
20. Gao, H.; Rose, J.L. Ice detection and classification on an aircraft wing with ultrasonic shear horizontal guided waves. *IEEE Trans. Ultrason. Ferroelectr. Freq. Control* **2009**, *56*, 334–344. [[PubMed](#)]
21. Saeed, F.; Algarni, A.Z. Analysis method for inertial particle separator. *J. Aircr.* **2007**, *44*, 1150–1158. [[CrossRef](#)]
22. Hasanzadeh, K.; Laurendeau, E.; Paraschivoiu, I. Quasi-Steady Convergence of Multistep Navier-Stokes Icing Simulations. *J. Aircr.* **2013**, *50*, 1261–1274. [[CrossRef](#)]
23. Kennedy, K.; Barriault, M. Treatment kinetics of aircraft deicing fluid in an anaerobic baffled reactor. *J. Environ. Eng. Sci.* **2007**, *6*, 11–17. [[CrossRef](#)]
24. McNeill, K.S.; Cancilla, D.A. Detection of triazole deicing additives in soil samples from airports with low, mid, and large volume aircraft deicing activities. *Bull. Environ. Contam. Toxicol.* **2009**, *82*, 265–269. [[CrossRef](#)] [[PubMed](#)]
25. Bernstein, B.C.; Omeron, T.A.; Politovich, M.K.; McDonough, F. Surface weather features associated with freezing precipitation and severe in-flight aircraft icing. *Atmos. Res.* **1998**, *46*, 57–73. [[CrossRef](#)]
26. Corsi, S.R.; Geis, S.W.; Loyo-Rosales, J.E.; Rice, C.P.; Sheesley, R.J.; Greg, G.; Failey, A.; Cancilla, D.A. Characterization of aircraft deicer and Anti-Icer components and toxicity in airport snowbanks and snowmelt runoff. *Environ. Sci. Technol.* **2006**, *40*, 3195–3202. [[CrossRef](#)] [[PubMed](#)]
27. Marin, J.; Kennedy, K.J.; Eskicioglu, C. Characterization of an anaerobic baffled reactor treating dilute aircraft de-icing fluid and long term effects of operation on granular biomass. *Bioresour. Technol.* **2010**, *101*, 2217–2223. [[CrossRef](#)] [[PubMed](#)]
28. Labeas, G.N.; Diamantakos, I.D.; Sunaric, M.M. Simulation of the electroimpulse de-icing process of aircraft wings. *J. Aircr.* **2006**, *43*, 1876–1885. [[CrossRef](#)]
29. Shen, Y.; Tao, H.; Chen, S.; Zhu, L.; Wang, T.; Tao, J. Icephobic/anti-icing potential of superhydrophobic Ti6Al4V surfaces with hierarchical textures. *RSC Adv.* **2014**, *5*, 1666–1672. [[CrossRef](#)]
30. Schrimpf, H.; Pfitzner, K. Aircraft Deicing or Antiicing Compositions. U.S. Patent 5759436, 2 June 1998.
31. Sun, Y.; Wang, G. Application of smith predictor in aircraft deicing vehicle delayed time-varying heating system. *J. Simul.* **2006**, *1*, 145–147.
32. Boinovich, L.B.; Emelyanenko, A.M.; Ivanov, V.K.; Pashinin, A.S. Durable icephobic coating for stainless steel. *ACS Appl. Mater. Interface* **2013**, *5*, 2549–2554. [[CrossRef](#)] [[PubMed](#)]
33. Shinkafi, A.; Lawson, C. Evaluating inflight ice protection methods for applications on next generation aircraft. *J. Aeronaut. Eng. Technol.* **2013**, *3*, 1–21.
34. Antonini, C.; Innocenti, M.; Horn, T.; Marengo, M.; Amirfazli, A. Understanding the effect of superhydrophobic coatings on energy reduction in anti-icing systems. *Cold Reg. Sci. Technol.* **2011**, *67*, 58–67. [[CrossRef](#)]
35. Guo, Z.; Liu, W.; Su, B.L. Superhydrophobic surfaces: From natural to biomimetic to functional. *J. Colloid Interface Sci.* **2011**, *353*, 335–355. [[CrossRef](#)] [[PubMed](#)]
36. Bandyopadhyay, S.; Dey, R.; Raj, M.K.; Bhandaru, N.; Mukherjee, R.; Chakraborty, S. Mixing characteristics in microchannels with biomimetic superhydrophobic (Lotus leaf replica) walls. *Microfluid. Nanofluid.* **2017**, *21*, 152. [[CrossRef](#)]
37. Ensikat, H.J.; Ditsche-Kuru, P.; Neinhuis, C.; Barthlott, W. Superhydrophobicity in perfection: The outstanding properties of the lotus leaf. *Beilstein J. Nanotechnol.* **2011**, *2*, 152–161. [[CrossRef](#)] [[PubMed](#)]
38. Liu, M.; Zheng, Y.; Zhai, J.; Jiang, L. Bioinspired super-antiwetting interfaces with special liquid-solid adhesion. *Acc. Chem. Res.* **2009**, *43*, 368–377. [[CrossRef](#)] [[PubMed](#)]
39. Farhadi, S.; Farzaneh, M.; Kulinich, S.A. Anti-icing performance of superhydrophobic surfaces. *Appl. Surf. Sci.* **2011**, *257*, 6264–6269. [[CrossRef](#)]
40. Chuppina, S.V. Anti-Icing gradient organosilicate coatings. *Glass Phys. Chem.* **2007**, *33*, 502–509. [[CrossRef](#)]
41. Cassie, A.B.D. Wettability of porous surfaces. *Trans. Faraday Soc.* **1944**, *40*, 546–551. [[CrossRef](#)]
42. Tostmann, H.; Dimasi, E.; Shpyrko, O.G.; Pershan, P.S.; Ocko, B.M.; Deutsch, M. Microscopic structure of the wetting film at the surface of liquid Ga-Bi alloys. *Phys. Rev. Lett.* **2000**, *84*, 4385–4388. [[CrossRef](#)] [[PubMed](#)]
43. Spitzner, D.; Bergmann, U.; Apelt, S.; Boucher, R.A.; Wiesmann, H.P. Reversible switching of icing properties on pyroelectric polyvinylidene fluoride thin film coatings. *Coatings* **2015**, *5*, 724–736. [[CrossRef](#)]

44. Bormashenko, E.; Starov, V. Impact of surface forces on wetting of hierarchical surfaces and contact angle hysteresis. *Colloid Polym. Sci.* **2013**, *291*, 343–346. [[CrossRef](#)]
45. Rupp, F.; Scheideler, L.; Olshanska, N.; De, W.M.; Wieland, M.; Geis-Gerstorfer, J. Enhancing surface free energy and hydrophilicity through chemical modification of microstructured titanium implant surfaces. *J. Biomed. Mater. Res. Part A* **2006**, *76*, 323–334. [[CrossRef](#)] [[PubMed](#)]
46. Janssen, D.; Palma, R.D.; Verlaak, S.; Heremans, P.; Dehaen, W. Static solvent contact angle measurements, surface free energy and wettability determination of various self-assembled monolayers on silicon dioxide. *Thin Solid Films* **2006**, *515*, 1433–1438. [[CrossRef](#)]
47. Huang, Y.W. Properties of several low surface energy coatings containing Silicon/Fluorine. *Chem. Adhes.* **2006**, *3*, 194–197.
48. Saleema, N.; Sarkar, D.K.; Gallant, D.; Paynter, R.W.; Chen, X.G. Chemical nature of superhydrophobic aluminum alloy surfaces produced via a One-Step process using Fluoroalkyl-Silane in a base medium. *ACS Appl. Mater. Interface* **2011**, *3*, 4775–4781. [[CrossRef](#)] [[PubMed](#)]
49. Nishino, T.; Meguro, M.; Nakamae, K.; Motonori, M.A.; Ueda, Y. The Lowest Surface Free Energy Based on -CF₃ Alignment. *Langmuir* **1999**, *15*, 4321–4323. [[CrossRef](#)]
50. Xiu, Y.; Zhu, L.; Hess, D.W.; Wong, C.P. Hierarchical silicon etched structures for controlled hydrophobicity/superhydrophobicity. *Nano Lett.* **2007**, *7*, 3388–3393. [[CrossRef](#)] [[PubMed](#)]
51. Verplanck, N.; Galopin, E.; Camart, J.C.; Thomy, V.; Coffinier, Y.; Boukherroub, R. Reversible electrowetting on superhydrophobic silicon nanowires. *Nano Lett.* **2007**, *7*, 813–817. [[CrossRef](#)] [[PubMed](#)]
52. Butt, H.J.; Golovko, D.S.; Bonaccorso, E. On the derivation of Young's equation for sessile drops: Nonequilibrium effects due to evaporation. *J. Phys. Chem. B* **2007**, *111*, 5277–5283. [[CrossRef](#)] [[PubMed](#)]
53. Bormashenko, E. Physics of solid-liquid interfaces: From the Young equation to the superhydrophobicity. *Low Temp. Phys.* **2016**, *42*, 622–635. [[CrossRef](#)]
54. Hazlett, R.D. Fractal applications: Wettability and contact angle. *J. Colloid Interface Sci.* **1990**, *137*, 527–533. [[CrossRef](#)]
55. Style, R.W.; Dufresne, E.R. Static wetting on deformable substrates, from liquids to soft solids. *Soft Matter* **2012**, *8*, 7177–7184. [[CrossRef](#)]
56. Mockenhaupt, B.; Ensikat, H.J.; Spaeth, M.; Barthlott, W. Superhydrophobicity of biological and technical surfaces under moisture condensation: Stability in relation to surface structure. *Langmuir* **2008**, *24*, 13591–13597. [[CrossRef](#)] [[PubMed](#)]
57. Wenzel, R.N. Surface roughness and contact angle. *J. Phys. Chem.* **1949**, *53*, 1466–1467. [[CrossRef](#)]
58. Jiang, L.; Zhao, Y.; Zhai, J. A lotus-leaf-like superhydrophobic surface: A porous microsphere/nanofiber composite film prepared by electrohydrodynamics. *Angew. Chem.* **2004**, *116*, 4338–4441. [[CrossRef](#)] [[PubMed](#)]
59. Orchard, M.J.; Kohonen, M.; Humphries, S. The influence of surface energy on the self-cleaning of insect adhesive devices. *J. Exp. Biol.* **2012**, *215*, 279–286. [[CrossRef](#)] [[PubMed](#)]
60. Liu, K.; Yao, X.; Jiang, L. Recent developments in bio-inspired special wettability. *Chem. Soc. Rev.* **2010**, *39*, 3240–3255. [[CrossRef](#)] [[PubMed](#)]
61. Barthlott, W.; Nakajima, A. Purity of the sacred lotus, or escape from contamination in biological surfaces. *Planta* **1997**, *202*, 1–8. [[CrossRef](#)]
62. Lafuma, A.; Quéré, D. Superhydrophobic states. *Nat. Mater.* **2003**, *2*, 457–460. [[CrossRef](#)] [[PubMed](#)]
63. Shiu, J.Y.; Kuo, C.W.; Peilin, C.A.; Mou, C.Y. Fabrication of tunable superhydrophobic surfaces by nanosphere lithography. *Chem. Mater.* **2004**, *16*, 561–564. [[CrossRef](#)]
64. Masashi, M.; Akira, N.; Akira, F.; Kazuhito, H.A.; Toshiya, W. Effects of the surface roughness on sliding angles of water droplets on superhydrophobic surfaces. *Langmuir* **2000**, *16*, 5754–5760.
65. Ma, M.; Hill, R.M. Superhydrophobic surfaces. *Curr. Opin. Colloid Interface Sci.* **2006**, *11*, 193–202. [[CrossRef](#)]
66. Bormashenko, E. Young, Boruvka-Neumann, Wenzel and Cassie-Baxter equations as the transversality conditions for the variational problem of wetting. *Colloid Surf. A* **2009**, *345*, 163–165. [[CrossRef](#)]
67. Yamaguchi, M.; Suzuki, S.; Sasaki, S.; Chiba, T.; Itoh, N.; Hoga, M. Fabrication of nano-periodic structures and modification of the Wenzel model to estimate contact angle. *Sens. Actuators A Phys.* **2014**, *212*, 87–92. [[CrossRef](#)]
68. Chandler, D. Hydrophobicity at small and large length scales. *J. Phys. Chem. B* **1999**, *103*, 4570–4577.
69. Sas, I.; Gorga, R.E.; Joines, J.A.; Thoney, K.A. Literature review on superhydrophobic self-cleaning surfaces produced by electrospinning. *J. Polym. Sci. Part B Polym. Phys.* **2012**, *50*, 824–845. [[CrossRef](#)]

70. Furmidge, C.G.L. Studies at phase interfaces. I. The sliding of liquid drops on solid surfaces and a theory for spray retention. *J. Colloid Sci.* **1962**, *17*, 309–324. [[CrossRef](#)]
71. Jung, Y.C.; Bhushan, B. Dynamic effects of bouncing water droplets on superhydrophobic surfaces. *Langmuir* **2008**, *24*, 6262–6269. [[CrossRef](#)] [[PubMed](#)]
72. Reyssat, M.; Richard, D.; Clanet, C.; Quéré, D. Dynamical superhydrophobicity. *Faraday Discuss.* **2010**, *146*, 19–33. [[CrossRef](#)] [[PubMed](#)]
73. Pierce, E.; Carmona, F.J.; Amirfazli, A. Understanding of sliding and contact angle results in tilted plate experiments. *Colloid Surf. A* **2008**, *323*, 73–82. [[CrossRef](#)]
74. Yoshimitsu, Z.; Nakajima, A.; Watanabe, T.; Hashimoto, K. Effects of surface structure on the hydrophobicity and sliding behavior of water droplets. *Langmuir* **2002**, *18*, 5818–5822. [[CrossRef](#)]
75. Wolfram, E.; Faust, R. *Wetting, Spreading, and Adhesion*; Academic Press: London, UK, 1978.
76. Nakajima, A.; Hashimoto, K.; Watanabe, T. Recent studies on super-hydrophobic films. *Monatshefte Chem.* **2001**, *132*, 31–41. [[CrossRef](#)]
77. Gao, L.; McCarthy, T.J. Contact angle hysteresis explained. *Langmuir* **2006**, *22*, 6234–6237. [[CrossRef](#)] [[PubMed](#)]
78. Johnson, R.E.; Dettre, R.H. Contact angle hysteresis. I. Study of an idealized rough surface. *Adv. Chem. Ser.* **1964**, *43*, 112–135.
79. Zheng, Q.S.; Yu, Y.; Zhao, Z.H. Effects of hydraulic pressure on the stability and transition of wetting modes of superhydrophobic surfaces. *Langmuir* **2005**, *21*, 12207–12212. [[CrossRef](#)] [[PubMed](#)]
80. Patankar, N.A. Transition between superhydrophobic states on rough surfaces. *Langmuir* **2004**, *20*, 7097–7102. [[CrossRef](#)] [[PubMed](#)]
81. Sun, M.; Luo, C.; Xu, L.; Ji, H.; Ouyang, Q.; Yu, D.; Chen, Y. Artificial lotus leaf by nanocasting. *Langmuir* **2005**, *21*, 8978–8981. [[CrossRef](#)] [[PubMed](#)]
82. Feng, L.; Li, S.; Li, Y.; Li, H.; Zhang, L.; Zhai, J.; Song, Y.; Liu, B.; Jiang, L.; Zhu, D. Super-Hydrophobic surfaces: From natural to artificial. *Adv. Mater.* **2002**, *14*, 1857–1860. [[CrossRef](#)]
83. Bormashenko, E.; Pogreb, R.; Whyman, G.; Erlich, M. Resonance Cassie-Wenzel wetting transition for horizontally vibrated drops deposited on a rough surface. *Langmuir* **2007**, *23*, 12217–12221. [[CrossRef](#)] [[PubMed](#)]
84. Spori, D.M.; Drobek, T.; Zürcher, S.; Spencer, N.D. Cassie-state wetting investigated by means of a hole-to-pillar density gradient. *Langmuir* **2010**, *26*, 9465–9473. [[CrossRef](#)] [[PubMed](#)]
85. Shen, Y.; Tao, J.; Tao, H.; Chen, S.; Pan, L.; Wang, T. Nanostructures in superhydrophobic Ti6Al4V hierarchical surfaces control wetting state transitions. *Soft Matter* **2015**, *11*, 3806–3811. [[CrossRef](#)] [[PubMed](#)]
86. Hsieh, C.T.; Wu, F.L.; Yang, S.Y. Superhydrophobicity from composite nano/microstructures: Carbon fabrics coated with silica nanoparticles. *Surf. Coat. Technol.* **2008**, *202*, 6103–6108. [[CrossRef](#)]
87. Tsai, P.; Pacheco, S.; Pirat, C.; Lefferts, L.; Lohse, D. Drop impact upon micro- and nanostructured superhydrophobic surfaces. *Langmuir* **2009**, *25*, 12293–12298. [[CrossRef](#)] [[PubMed](#)]
88. Bormashenko, E.; Pogreb, R.; Stein, T.; Whyman, G.; Erlich, M.; Musin, A.; Machavariani, V.; Aurbach, D. Characterization of rough surfaces with vibrated drops. *Phys. Chem. Chem. Phys.* **2008**, *10*, 4056–4061. [[CrossRef](#)] [[PubMed](#)]
89. Whyman, G.; Bormashenko, E. How to make the Cassie wetting state stable? *Langmuir* **2011**, *27*, 8171–8176. [[CrossRef](#)] [[PubMed](#)]
90. Tran, T.; Staat, H.J.J.; Susarreyarce, A.; Foertsch, T.C.; Van Houselt, A.; Gardeniers, H.J.G.E.; Prosperetti, A.; Lohse, D.; Sun, C. Droplet impact on superheated micro-structured surfaces. *Soft Matter* **2013**, *9*, 3272–3282. [[CrossRef](#)]
91. Hozumi, A.; Kim, B.; McCarthy, T.J. Hydrophobicity of perfluoroalkyl isocyanate monolayers on oxidized aluminum surfaces. *Langmuir* **2009**, *25*, 6834–6840. [[CrossRef](#)] [[PubMed](#)]
92. Yan, Y.Y.; Gao, N.; Barthlott, W. Mimicking natural superhydrophobic surfaces and grasping the wetting process: A review on recent progress in preparing superhydrophobic surfaces. *Adv. Colloid Interface Sci.* **2011**, *169*, 80–105. [[CrossRef](#)] [[PubMed](#)]
93. Berendsen, C.W.J.; Škřeň, M.; Najdek, D.; Černý, F. Superhydrophobic surface structures in thermoplastic polymers by interference lithography and thermal imprinting. *Appl. Surf. Sci.* **2009**, *255*, 9305–9310. [[CrossRef](#)]

94. Accardo, A.; Gentile, F.; Mecarini, F.; Angelis, F.D.; Burghammer, M.; Fabrizio, E.D.; Riekkel, C. Ultrahydrophobic PMMA micro- and nano-textured surfaces fabricated by optical lithography and plasma etching for X-ray diffraction studies. *Microelectron. Eng.* **2011**, *88*, 1660–1663. [[CrossRef](#)]
95. Choi, J.; Cho, W.; Jung, Y.S.; Hong, S.K.; Kim, H.T. Direct fabrication of micro/nano-patterned surfaces by vertical-directional photofluidization of azobenzene materials. *ACS Nano* **2017**, *11*, 1320–1327. [[CrossRef](#)] [[PubMed](#)]
96. Lee, S.M.; Song, J.H.; Jung, P.G.; Jang, D.H.; Kim, S.M.; Jeong, W.B.; Kim, B.M.; Ko, J.S. Nanotextured superhydrophobic micromesh. *Sens. Actuators A Phys.* **2011**, *171*, 233–240. [[CrossRef](#)]
97. Wang, J.; Song, X.; Li, R.; Shen, J.; Yang, G.; Huang, H. Fluorocarbon thin film with superhydrophobic property prepared by pyrolysis of hexafluoropropylene oxide. *Appl. Surf. Sci.* **2012**, *258*, 9782–9785. [[CrossRef](#)]
98. Goswami, D.; Medda, S.K.; De, G. Superhydrophobic films on glass surface derived from trimethylsilanized silica gel nanoparticles. *ACS Appl. Mater. Interface* **2011**, *3*, 3440–3447. [[CrossRef](#)] [[PubMed](#)]
99. Kato, S.; Sato, A. Micro/nanotextured polymer coatings fabricated by UV curing-induced phase separation: Creation of superhydrophobic surfaces. *J. Mater. Chem.* **2012**, *22*, 8613–8621. [[CrossRef](#)]
100. Meng, J.; Lin, S.; Xiong, X. Preparation of breathable and superhydrophobic coating film via spray coating in combination with vapor-induced phase separation. *Prog. Org. Coat.* **2017**, *107*, 29–36. [[CrossRef](#)]
101. Song, J.; Xu, W.; Liu, X.; Lu, Y.; Wei, Z.; Wu, L. Ultrafast fabrication of rough structures required by superhydrophobic surfaces on Al substrates using an immersion method. *Chem. Eng. J.* **2012**, *211*, 143–152. [[CrossRef](#)]
102. Wu, J.; Wang, N.; Wang, L.; Dong, H.; Zhao, Y.; Jiang, L. Electrospun porous structure fibrous film with high oil adsorption capacity. *ACS Appl. Mater. Interfaces* **2012**, *4*, 3207–3212. [[CrossRef](#)] [[PubMed](#)]
103. Utech, S.; Bley, K.; Aizenberg, J.; Vogel, N. Tailoring re-entrant geometry in inverse colloidal monolayers to control surface wettability. *J. Mater. Chem. A* **2016**, *4*, 6853–6859. [[CrossRef](#)]
104. Hou, W.; Wang, Q. Stable polytetrafluoroethylene superhydrophobic surface with lotus-leaf structure. *J. Colloid Interface Sci.* **2009**, *333*, 400–403. [[CrossRef](#)] [[PubMed](#)]
105. Zhu, M.; Gao, H.; Li, H.; Xu, J.; Chen, Y. A facile processing way of silica needle arrays with tunable orientation by tube arrays fabrication and etching method. *J. Solid State Chem.* **2010**, *183*, 595–599. [[CrossRef](#)]
106. Sarkar, D.K.; Farzaneh, M.; Paynter, R.W. Superhydrophobic properties of ultrathin rf-sputtered Teflon films coated etched aluminum surfaces. *Mater. Lett.* **2008**, *62*, 1226–1229. [[CrossRef](#)]
107. Lai, Y.; Lin, L.; Pan, F.; Huang, J.; Song, R.; Huang, Y.; Lin, C.; Fuchs, H.; Chi, L. Bioinspired patterning with extreme wettability contrast on TiO₂ nanotube array surface: A versatile platform for biomedical applications. *Small* **2013**, *9*, 2945–2953. [[CrossRef](#)] [[PubMed](#)]
108. Lai, Y.; Lin, C.; Wang, H.; Huang, J.; Zhuang, H.; Sun, L. Superhydrophilic-superhydrophobic micropattern on TiO₂ nanotube films by photocatalytic lithography. *Electrochem. Commun.* **2008**, *10*, 387–391. [[CrossRef](#)]
109. Tan, J.; Hao, J.; An, Z.; Liu, C. Superhydrophobic surfaces on brass substrates fabricated via micro-etching and a growth process. *RSC Adv.* **2017**, *7*, 26145–26152. [[CrossRef](#)]
110. Guo, L.; Yuan, W.; Li, J.; Zhang, Z.; Xie, Z. Stable superhydrophobic surfaces over a wide pH range. *Appl. Surf. Sci.* **2008**, *254*, 2158–2161. [[CrossRef](#)]
111. Tang, Y.; Zhang, Q.; Zhan, X.; Chen, F. Superhydrophobic and anti-icing properties at overcooled temperature of a fluorinated hybrid surface prepared via a sol-gel process. *Soft Matter* **2015**, *11*, 4540–4550. [[CrossRef](#)] [[PubMed](#)]
112. Lu, S.; Chen, Y.; Xu, W.; Liu, W. Controlled growth of superhydrophobic films by sol-gel method on aluminum substrate. *Appl. Surf. Sci.* **2010**, *256*, 6072–6075. [[CrossRef](#)]
113. Dong, F.; Xie, H.; Zheng, Q.; Ha, C.S. Superhydrophobic polysilsesquioxane/polystyrene microspheres with controllable morphology: From raspberry-like to flower-like structure. *RSC Adv.* **2017**, *7*, 6685–6690. [[CrossRef](#)]
114. Wang, S.; Feng, L.; Jiang, L. One-step solution-immersion process for the fabrication of stable bionic superhydrophobic surfaces. *Adv. Mater.* **2006**, *18*, 767–770. [[CrossRef](#)]
115. Ma, M.; Mao, Y.; Gupta, M.; Gleason, K.K.; Rutledge, G.C. Superhydrophobic fabrics produced by electrospinning and chemical vapor deposition. *Macromolecules* **2005**, *38*, 9742–9748. [[CrossRef](#)]

116. Ouyang, S.; Wang, T.; Yu, Y.; Yang, B.; Yao, J.; Wang, S. From Trans to Cis Conformation: Further Understanding the Surface Properties of Poly(*m*-Phenylene isophthalamide). *ACS Omega* **2017**, *2*, 290–298. [[CrossRef](#)]
117. Rezaei, S.; Manoucheri, I.; Moradian, R.; Pourabbas, B. One-step chemical vapor deposition and modification of silica nanoparticles at the lowest possible temperature and superhydrophobic surface fabrication. *Chem. Eng. J.* **2014**, *252*, 11–16. [[CrossRef](#)]
118. Kontziampasis, D.; Boulousis, G.; Smyrnakis, A.; Ellinas, K.; Tserepi, A.; Gogolides, E. Biomimetic, antireflective, superhydrophobic and oleophobic PMMA and PMMA-coated glass surfaces fabricated by plasma processing. *Microelectron. Eng.* **2014**, *121*, 33–38. [[CrossRef](#)]
119. Li, Y.; Zheng, M.; Ma, L.; Zhong, M.; Shen, W. Fabrication of hierarchical ZnO architectures and their superhydrophobic surfaces with strong adhesive force. *Inorg. Chem.* **2008**, *47*, 3140–3143. [[CrossRef](#)] [[PubMed](#)]
120. Wang, X.; Zuo, J.; Keil, P.; Grundmeier, G. Comparing the growth of PVD silver nanoparticles on ultra thin fluorocarbon plasma polymer films and self-assembled fluoroalkyl silane monolayers. *Nanotechnology* **2007**, *18*, 265303. [[CrossRef](#)] [[PubMed](#)]
121. Zhu, L.; Tao, J.; Tao, H.; Chen, S.; Shen, Y.; Xu, A.; Jiang, J.J.; Pan, L. In-situ growth of Cu₂ZnSnS₄ nanosheets on TiO₂ nanowires for Enhanced Photoelectrochemical Performance. *J. Alloy Compd.* **2015**, *649*, 704–711. [[CrossRef](#)]
122. Yamauchi, G.; Miller, J.D.; Saito, H.; Takai, K.; Ueda, T.; Takazawa, H.; Yamamoto, H.; Nisli, S. Wetting characteristics of newly developed water-repellent material. *Colloid Surf. A* **1996**, *116*, 125–134. [[CrossRef](#)]
123. Soeno, T.; Inokuchi, K.; Shiratori, S. Ultra-water-repellent surface: Fabrication of complicated structure of SiO₂ nanoparticles by electrostatic self-assembled films. *Appl. Surf. Sci.* **2004**, *237*, 539–543. [[CrossRef](#)]
124. Yelash, L.; Virnau, P.; Binder, K.; Paul, W. Slow process in confined polymer melts: Layer exchange dynamics at a polymer solid interface. *Phys. Rev. E* **2010**, *82*, 50801. [[CrossRef](#)] [[PubMed](#)]
125. Weickgenannt, C.M.; Zhang, Y.; Lembach, A.N.; Roisman, I.V.; Gambaryan-Roisman, T.; Yarin, A.L.; Tropea, C. Nonisothermal drop impact and evaporation on polymer nanofiber mats. *Phys. Rev. E* **2011**, *83*, 36305. [[CrossRef](#)] [[PubMed](#)]
126. Zang, D.; Wang, X.; Geng, X.; Zhang, Y.; Chen, Y. Impact dynamics of droplets with silica nanoparticles and polymer additives. *Soft Matter* **2012**, *9*, 394–400. [[CrossRef](#)]
127. Wang, Y.; Amberg, G.; Carlson, A. Local dissipation limits the dynamics of impacting droplets on smooth and rough substrates. *Phys. Rev. Fluids* **2017**, *2*, 33602. [[CrossRef](#)]
128. Wang, L.; Gong, Q.; Zhan, S.; Jiang, L.; Zheng, Y. Robust Anti-Icing performance of a flexible superhydrophobic surface. *Adv. Mater.* **2016**, *28*, 7729–7735. [[CrossRef](#)] [[PubMed](#)]
129. Wu, H.; Lin, Y.B.; Gong, J.J.; Zhang, F.; Zeng, M.; Qin, M.H.; Zhang, Z.; Ru, Q.; Liu, Z.W.; Gao, X.S. Significant enhancements of dielectric and magnetic properties in Bi(Fe_{1-x}Mg_x)O_{3-x/2} induced by oxygen vacancies. *J. Phys. D Appl. Phys.* **2013**, *46*, 145001. [[CrossRef](#)]
130. Ramachandran, R.; Sobolev, K.; Nosonovsky, M. Dynamics of droplet impact on Hydrophobic/Icephobic concrete with the potential for superhydrophobicity. *Langmuir* **2015**, *31*, 1437–1444. [[CrossRef](#)] [[PubMed](#)]
131. Ruiter, J.D.; Lagrauw, R.; Ende, D.V.D.; Mugele, F. Wettability-independent bouncing on flat surfaces mediated by thin air films. *Nat. Phys.* **2015**, *11*, 48–53. [[CrossRef](#)]
132. Kim, H.; Lee, C.; Kim, M.H.; Kim, J. Drop impact characteristics and structure effects of hydrophobic surfaces with micro- and/or nanoscaled structures. *Langmuir* **2012**, *28*, 11250–11257. [[CrossRef](#)] [[PubMed](#)]
133. Lee, J.B.; Derome, D.; Dolatabadi, A.; Carmeliet, J. Energy budget of liquid drop impact at maximum spreading: Numerical simulations and experiments. *Langmuir* **2016**, *32*, 1279–1288. [[CrossRef](#)] [[PubMed](#)]
134. Martin, A.; Lars, Ö.; Sten, L.; Anders, P. Preparation of nanosize anatase and rutile TiO₂ by hydrothermal treatment of microemulsions and their activity for photocatalytic wet oxidation of phenol. *J. Phys. Chem. B* **2014**, *106*, 10674–10679.
135. Li, Z.; Kong, Q.; Ma, X.; Zang, D.; Guan, X.; Ren, X. Dynamic effects and adhesion of water droplet impact on hydrophobic surfaces: Bouncing or sticking. *Nanoscale* **2017**, *9*, 8249–8255. [[CrossRef](#)] [[PubMed](#)]
136. Baek, S.; Kim, W.; Jeon, S.; Yong, K. Dual dimensional nanostructures with highly durable non-wetting properties under dynamic and underwater conditions. *Nanoscale* **2017**, *9*, 6665–6673. [[CrossRef](#)] [[PubMed](#)]
137. Dash, S.; Alt, M.T.; Garimella, S.V. Hybrid surface design for robust superhydrophobicity. *Langmuir* **2012**, *28*, 9606–9615. [[CrossRef](#)] [[PubMed](#)]

138. Bird, J.C.; Dhiman, R.; Kwon, H.M.; Varanasi, K.K. Reducing the contact time of a bouncing drop. *Nature* **2013**, *503*, 385–388. [[CrossRef](#)] [[PubMed](#)]
139. Kwak, G.; Lee, M.; Senthil, K.; Yong, K. Wettability control and water droplet dynamics on SiC-SiO₂ core-shell nanowires. *Langmuir* **2010**, *26*, 12273–12277. [[CrossRef](#)] [[PubMed](#)]
140. Shen, Y.; Liu, S.; Zhu, C.; Tao, J.; Wang, G. Facile fabrication of hierarchical structured superhydrophobic surface and its ultra dynamic water repellency. *Chem. Eng. J.* **2016**, *313*, 47–55. [[CrossRef](#)]
141. Shen, Y.; Liu, S.; Zhu, C.; Tao, J.; Chen, Z.; Tao, H.; Pan, L.; Wang, G.; Wang, T. Bouncing dynamics of impact droplets on the convex superhydrophobic surfaces. *Appl. Phys. Lett.* **2017**, *110*, 221601. [[CrossRef](#)]
142. Wen, L.; Tian, Y.; Jiang, L. Bioinspired Super-wettability from fundamental research to practical applications. *Angew. Chem. Int. Ed.* **2015**, *54*, 3387–3399. [[CrossRef](#)] [[PubMed](#)]
143. Wang, P.; Qiu, R.; Zhang, D.; Lin, Z.; Hou, B. Fabricated super-hydrophobic film with potentiostatic electrolysis method on copper for corrosion protection. *Electrochim. Acta* **2011**, *56*, 517–522. [[CrossRef](#)]
144. Varanasi, K.K.; Deng, T.; Smith, J.D.; Hus, M.; Bhate, N. Frost formation and ice adhesion on superhydrophobic surfaces. *Appl. Phys. Lett.* **2010**, *97*, 234102. [[CrossRef](#)]
145. He, M.; Zhang, Q.; Zeng, X.; Cui, D.; Chen, J.; Li, H.; Wang, J.; Song, Y. Hierarchical porous surface for efficiently controlling microdroplets' self-removal. *Adv. Mater.* **2013**, *25*, 2291–2295. [[CrossRef](#)] [[PubMed](#)]
146. Lai, Y.; Tang, Y.; Gong, J.; Gong, D.; Chi, L.; Lin, C.; Chen, Z. Transparent superhydrophobic/superhydrophilic TiO₂-based coatings for self-cleaning and anti-fogging. *J. Mater. Chem.* **2012**, *22*, 7420–7426. [[CrossRef](#)]
147. Bauer, S.; Park, J.; Mark, K.V.D.; Schmuki, P. Improved attachment of mesenchymal stem cells on super-hydrophobic TiO₂ nanotubes. *Acta Biomater.* **2008**, *4*, 1576–1582. [[CrossRef](#)] [[PubMed](#)]
148. Ishizaki, T.; Saito, N.; Takai, O. Correlation of cell adhesive behaviors on superhydrophobic, superhydrophilic, and micropatterned superhydrophobic/superhydrophilic surfaces to their surface chemistry. *Langmuir* **2010**, *26*, 8147–8154. [[CrossRef](#)] [[PubMed](#)]
149. Hasan, J.; Webb, H.K.; Truong, V.K.; Pogodin, S.; Baulin, V.A.; Watson, G.S.; Watson, J.A.; Crawford, R.J.; Ivanova, E.P. Selective bactericidal activity of nanopatterned superhydrophobic cicada Psaltoda claripennis wing surfaces. *Appl. Microbiol. Biotechnol.* **2013**, *97*, 9257–9262. [[CrossRef](#)] [[PubMed](#)]
150. Ivanova, E.P.; Hasan, J.; Webb, H.K.; Truong, V.K.; Watson, G.S.; Watson, J.A.; Baulin, V.A.; Pogodin, S.; Wang, J.Y.; Tobin, M.J. Natural bactericidal surfaces: Mechanical rupture of Pseudomonas aeruginosa cells by cicada wings. *Small* **2012**, *8*, 2489–2494. [[CrossRef](#)] [[PubMed](#)]
151. Zhao, L.; Liu, Q.; Gao, R.; Wang, J.; Yang, W.; Liu, L. One-step method for the fabrication of superhydrophobic surface on magnesium alloy and its corrosion protection, antifouling performance. *Corros. Sci.* **2014**, *80*, 177–183. [[CrossRef](#)]
152. Lin, F.D.; Li, S.H.; Li, H.J.; Jin, Z.D.; Song, Y.L.; Jiang, L. Super-hydrophobic surface of aligned polyacrylonitrile nanofibers. *Angew. Chem.* **2002**, *114*, 1269–1271.
153. Lai, Y.; Gao, X.; Zhuang, H.; Huang, J.; Lin, C.; Jiang, L. Designing superhydrophobic porous nanostructures with tunable water adhesion. *Adv. Mater.* **2009**, *21*, 3799–3803. [[CrossRef](#)]
154. Cheng, Z.; Feng, L.; Jiang, L. Tunable adhesive superhydrophobic surfaces for superparamagnetic microdroplets. *Adv. Funct. Mater.* **2010**, *18*, 3219–3225. [[CrossRef](#)]
155. Cao, L.; Jones, A.K.; Sikka, V.K.; Wu, J.; Gao, D. Anti-icing superhydrophobic coatings. *Langmuir* **2009**, *25*, 12444–12448. [[CrossRef](#)] [[PubMed](#)]
156. Metya, A.K.; Singh, J.K.; Müller-Plathe, F. Ice nucleation on nanotextured surfaces: The influence of surface fraction, pillar height and wetting states. *Phys. Chem. Chem. Phys.* **2016**, *18*, 26796–26806. [[CrossRef](#)] [[PubMed](#)]
157. Abyzov, A.S.; Schmelzer, J.W.P.; Davydov, L.N. Heterogeneous nucleation on rough surfaces: Generalized Gibbs's approach. *J. Chem. Phys.* **2017**, *147*, 214705. [[CrossRef](#)] [[PubMed](#)]
158. He, M.; Li, H.; Wang, J.; Song, Y. Superhydrophobic surface at low surface temperature. *Appl. Phys. Lett.* **2011**, *98*, 93118. [[CrossRef](#)]
159. Miljkovic, N.; Enright, R.; Nam, Y.; Lopez, K.; Dou, N.; Sack, J.; Wang, E.N. Jumping-droplet-enhanced condensation on scalable superhydrophobic nanostructured surfaces. *Nano Lett.* **2012**, *13*, 179–187. [[CrossRef](#)] [[PubMed](#)]
160. Wen, M.; Wang, L.; Zhang, M.; Jiang, L.; Zheng, Y. Antifogging and icing-delay properties of composite micro- and nanostructured surfaces. *ACS Appl. Mater. Interface* **2014**, *6*, 3963–3968. [[CrossRef](#)] [[PubMed](#)]

161. Boinovich, L.B.; Emelyanenko, A.M. Anti-icing potential of superhydrophobic coatings. *Mendeleev Commun.* **2013**, *23*, 3–10. [[CrossRef](#)]
162. Hao, P.; Lv, C.; Zhang, X. Freezing of sessile water droplets on surfaces with various roughness and wettability. *Appl. Phys. Lett.* **2014**, *104*, 161609. [[CrossRef](#)]
163. Darmanin, T.; Guittard, F. Recent advances in the potential applications of bioinspired superhydrophobic materials. *J. Mater. Chem. A* **2014**, *2*, 16319–16359. [[CrossRef](#)]
164. Karmouch, R.; Ross, G.G. Experimental study on the evolution of contact angles with temperature near the freezing point. *J. Phys. Chem. C* **2010**, *114*, 4063–4066. [[CrossRef](#)]
165. Guo, P.; Zheng, Y.; Wen, M.; Song, C.; Lin, Y.; Jiang, L. Icephobic/anti-icing properties of micro/nanostructured surfaces. *Adv. Mater.* **2012**, *24*, 2642–2648. [[CrossRef](#)] [[PubMed](#)]
166. Tourkine, P.; Le, M.M.; Quéré, D. Delayed freezing on water repellent materials. *Langmuir* **2009**, *25*, 7214–7216. [[CrossRef](#)] [[PubMed](#)]
167. Shen, Y.; Tao, J.; Tao, H.; Chen, S.; Pan, L.; Wang, T. Superhydrophobic Ti6Al4V surfaces with regular array patterns for anti-icing applications. *RSC Adv.* **2015**, *5*, 32813–32818. [[CrossRef](#)]
168. Li, K.; Xu, S.; Shi, W.; He, M.; Li, H.; Li, S.; Zhou, X.; Wang, J.; Song, Y. Investigating the effects of solid surfaces on ice nucleation. *Langmuir* **2012**, *28*, 10749–10754. [[CrossRef](#)] [[PubMed](#)]
169. Chen, D.; Gelenter, M.D.; Hong, M.; Cohen, R.E.; McKinley, G.H. Icephobic surfaces induced by interfacial non-frozen water. *ACS Appl. Mater. Interface* **2017**, *9*, 4202–4214. [[CrossRef](#)] [[PubMed](#)]
170. Yong, H.Y.; Wang, C.; Wynne, K.J.; Gupta, M.C. Oil-Infused superhydrophobic silicone material for low ice adhesion with long term infusion stability. *ACS Appl. Mater. Interface* **2016**, *8*, 32050–32059. [[CrossRef](#)] [[PubMed](#)]
171. Ruan, M.; Li, W.; Wang, B.; Deng, B.; Ma, F.; Yu, Z. Preparation and anti-icing behavior of superhydrophobic surfaces on aluminum alloy substrates. *Langmuir* **2013**, *29*, 8482–8491. [[CrossRef](#)] [[PubMed](#)]
172. Wang, Y.; Xue, J.; Wang, Q.; Chen, Q.; Ding, J. Verification of icephobic/anti-icing properties of a superhydrophobic surface. *ACS Appl. Mater. Interface* **2013**, *5*, 3370–3381. [[CrossRef](#)] [[PubMed](#)]
173. Huang, L.; Liu, Z.; Liu, Y.; Gou, Y. Preparation and anti-frosting performance of super-hydrophobic surface based on copper foil. *Int. J. Therm. Sci.* **2011**, *50*, 432–439. [[CrossRef](#)]
174. Lo, C.W.; Sahoo, V.; Lu, M.C. Control of ice formation. *ACS Nano* **2017**, *11*, 2665–2674. [[CrossRef](#)] [[PubMed](#)]
175. Wilson, P.W.; Lu, W.; Xu, H.; Kim, P.; Kreder, M.J.; Alvarenga, J.; Aizenberg, J. Inhibition of ice nucleation by slippery liquid-infused porous surfaces (SLIPS). *Phys. Chem. Chem. Phys.* **2013**, *15*, 581–585. [[CrossRef](#)] [[PubMed](#)]
176. Wang, N.; Xiong, D.; Pan, S.; Wang, K.; Shi, Y.; Deng, Y. Robust superhydrophobic coating and the anti-icing study of its lubricants-infused-composited surface under condensing condition. *New J. Chem.* **2017**, *41*, 1846–1853. [[CrossRef](#)]
177. Kim, P.; Wong, T.S.; Alvarenga, J.; Kreder, M.J.; Adornomartinez, W.E.; Aizenberg, J. Liquid-Infused nanostructured surfaces with extreme Anti-Ice and Anti-Frost performance. *ACS Nano* **2012**, *6*, 6569–6577. [[CrossRef](#)] [[PubMed](#)]
178. Liu, Y.; Whyman, G.; Bormashenko, E.; Hao, C.; Wang, Z. Controlling drop bouncing using surfaces with gradient features. *Appl. Phys. Lett.* **2015**, *107*, 51604. [[CrossRef](#)]
179. Liu, Y.; Moevius, L.; Xu, X.; Qian, T.; Yeomans, J.M.; Wang, Z. Pancake bouncing on superhydrophobic surfaces. *Nat. Phys.* **2014**, *10*, 515–519. [[CrossRef](#)] [[PubMed](#)]
180. Que, L.; Zhang, L.; Wu, W.; Wu, J.; Lin, J.; Huang, M. High-efficiency dye-sensitized solar cells based on ultra-long single crystalline titanium dioxide nanowires. *J. Power Sources* **2014**, *266*, 440–447. [[CrossRef](#)]
181. Chernyy, S.; Järn, M.; Shimizu, K.; Swerin, A.; Pedersen, S.U.; Daasbjerg, K.; Makkonen, L.; Claesson, P.; Iruthayaraj, J. Superhydrophilic polyelectrolyte brush layers with imparted Anti-Icing properties: Effect of counter ions. *ACS Appl. Mater. Interface* **2014**, *6*, 6487–6496. [[CrossRef](#)] [[PubMed](#)]
182. Ostendorf, D.W.; Rotaru, C.; Hinlein, E.S. Steady groundwater transport of highway deicing agent constituents from an infiltration basin. *J. Irrig. Drain. Eng.* **2008**, *134*, 630–637. [[CrossRef](#)]
183. Wu, X.J.; Li, Q.X.; Huang, J.; Yang, J.L. Theoretical study on the electron transport properties of single molecular bridge. *Acta Phys. Chim. Sin.* **2004**, *20*, 995–1002.
184. Chen, J.; Liu, J.; He, M.; Li, K.; Cui, D.; Zhang, Q.; Zeng, X.; Zhang, Y.; Wang, J.; Song, Y. Superhydrophobic surfaces cannot reduce ice adhesion. *Appl. Phys. Lett.* **2012**, *101*, 111603. [[CrossRef](#)]

185. Jung, S.; Dorrestijn, M.; Raps, D.; Das, A.; Megaridis, C.M.; Poulikakos, D. Are superhydrophobic surfaces best for icephobicity? *Langmuir* **2011**, *27*, 3059–3066. [[CrossRef](#)] [[PubMed](#)]
186. Nosonovsky, M.; Hejazi, V. Why superhydrophobic surfaces are not always icephobic. *ACS Nano* **2012**, *6*, 8488–8491. [[CrossRef](#)] [[PubMed](#)]
187. Hejazi, V.; Sobolev, K.; Nosonovsky, M. From superhydrophobicity to icephobicity: Forces and interaction analysis. *Sci. Rep.* **2013**, *3*, 2194. [[CrossRef](#)] [[PubMed](#)]



© 2018 by the authors. Licensee MDPI, Basel, Switzerland. This article is an open access article distributed under the terms and conditions of the Creative Commons Attribution (CC BY) license (<http://creativecommons.org/licenses/by/4.0/>).